Title	Electron scale magnetic reconnections in laser produced plasmas
Author(s)	Kuramitsu, Yasuhiro; Sakai, Kentaro; Moritaka, Toseo
Citation	Reviews of Modern Plasma Physics. 2023, 7(1)
Version Type	AM
URL	https://hdl.handle.net/11094/91746
rights	
Note	

Electron scale magnetic reconnections in laser produced plasmas

Yasuhiro Kuramitsu[1,2*], Kentaro Sakai[1,2†] and Toseo Moritaka[3†]

[1*]Graduate School of Engineering, Osaka University, 2-1 Yamadaoka, Suita, 565-0871, Osaka, Japan.
[2]Institute of Laser Engineering, Osaka University, 2-6 Yamadaoka, Suita, 565-0871, Osaka, Japan.
[3]Department of Helical Plasma Research, National Institute for Fusion Science, 322-6 Oroshi-cho, Toki, 509-5292, Gifu, Japan.

*Corresponding author(s). E-mail(s): kuramitsu@eei.eng.osaka-u.ac.jp;
Contributing authors: kentaro.sakai@eie.eng.osaka-u.ac.jp; moritaka.toseo@nifs.ac.jp;
[†]These authors contributed equally to this work.

Abstract

Magnetic reconnection is a fundamental process in the universe, in which magnetic field energy is converted into plasma kinetic energy associated with a topological change in the magnetic field. Magnetic reconnections have been extensively investigated in space in the form of solar terrestrial plasmas, and also in laboratories in the form of magnetic confinement plasmas and laser-produced plasmas. Macroscopic features of magnetic reconnections can be well described in the context of magnetohydrodynamics (MHD) across a wide variety of research fields. However, how the kinetic regime of magnetic reconnection should be connected to the macroscopic MHD regime is still an open question. It is generally assumed that electron dynamics play an essential role in the triggering mechanism of magnetic reconnections. In this review, we discuss magnetic reconnections on the electron scale, focusing in particular on laboratory experiments using high-power lasers.

Keywords: Magnetic reconnection, Laser, Electron dynamics, Laboratory astrophysics

1 Introduction

Magnetic reconnection is fundamental to various phenomena in the universe such as aurorae, magnetospheric substorms, solar and stellar flares, winds, and coronal heating. For instance, magnetic reconnection on the solar surface releases the magnetic field energy as a plasma outflow, resulting in a contribution to the solar wind. The magnetic field of the solar wind and the Earth's magnetic field can reconnect on the day side of the magnetosphere, transferring solar wind energy to the magnetosphere. This in turn enhances the elongated magnetic field configuration and equivalently the current of the night-side magnetosphere or magnetotail. The elongated magnetic field forms an anti-parallel magnetic configuration, a magnetic neutral line, and a thin current sheet to support the anti-parallel magnetic configuration. When the current sheet becomes thinner than the typical ion gyroradius, the ions can no longer carry the current but the electrons can, supporting the elongated magnetic field. When the current sheet becomes even thinner than the electron gyroradius, nothing can carry the current and the current circuit in the magnetosphere is consequently disrupted. This is the onset of magnetic reconnection. The elongated magnetic field tries to return to a dipole-like magnetic field with a plasma flow toward the Earth. The plasma outflow propagates along the magnetic field and becomes the origin of the aurorae. It is believed that electron dynamics are essential to the triggering mechanism of magnetic reconnections (Horiuchi and Sato, 1997; Ishizawa et al., 2004; Zenitani et al., 2011; Yamada, 2022). However, the electron scale is tiny in space and time, and it is highly challenging to observe electron-scale phenomena in the universe.

The Magnetospheric Multiscale Mission (MMS) has provided electron-scale measurements of magnetic reconnection in the Earth's magnetosphere (Burch et al., 2016). Magnetic reconnection driven by electron-scale dynamics has been directly observed by in-situ MMS measurements in the magnetopause for the first time (Burch et al., 2016a). The electron acceleration produced by a single Fermi reflection along the magnetic field in magnetic reconnections has also been observed (Mozer et al., 2016). The MMS has also shown that electron jets near the electron diffusion region are relevant to magnetic reconnection in the magnetosheath, where the parallel electric field accelerates and heats the electrons and the electron pressure sustains the electric field (Wilder et al., 2017). The MMS has also revealed small-scale, complex dynamic structures by measuring electron dynamics (Russell et al., 2017). Phan et al. reported on electron magnetic reconnection without the coupling of ion dynamics in Earth's turbulent magnetosheath (Phan et al., 2018). Electron-scale magnetic reconnection has been observed with MMS not only on the day side but also on the night side of the magnetosphere, the magnetotail, where electrons flowing with the electron Alfvénic speed defined by the electron mass and density are also found (Torbert et al., 2018).

Direct in-situ measurements of electron-scale magnetic reconnection in space have been successful and have enriched our understanding of the plasma

nature of the microscopic electron dynamics governing macroscopic phenomena like magnetic reconnection. In-situ observations of solar-terrestrial plasmas reveal microscopic plasma processes but not the corresponding global structures. On the contrary, astrophysical observations determine the global structures of phenomena but not local information. Laboratory experiments can be a complementary approach for investigating magnetic reconnections because they allow the global structures of plasmas and the local plasma and field properties to be obtained simultaneously. Furthermore, the energy distribution functions of plasmas can also be obtained in laboratory experiments and the external magnetic field is controllable (Kuramitsu et al., 2012). Such simultaneous observations of local and global features of plasmas and fields in a controlled manner are never accessible in space and astrophysical observations, and thus, laboratory experiments can be a unique and powerful tool with which to investigate space and astrophysical phenomena such as magnetic reconnections (Takabe and Kuramitsu, 2021).

There have been excellent reviews on magnetic reconnections more generally, covering space and laboratory plasmas, including magnetic confinement plasmas (Yamada et al., 2010) and magnetic reconnections in laser-produced plasmas using laser-generated magnetic fields (Zhong et al., 2018). In this review, we focus on our recent efforts concerning magnetic reconnections driven by electron dynamics using high-power lasers. In Sec. 2, we briefly summarize the theoretical background of magnetic reconnection, paying special attention to the multiscale nature of magnetic reconnections. Since there is always a self-generated magnetic field in such experiments, we briefly review the Biermann magnetic field in Sec. 3. In Sec. 4, we discuss plasma propagation in the presence of external magnetic fields with magnetic field strength and magnetic field orientations. We discuss the global observations of magnetic reconnection driven by electron dynamics in Sec. 5, and the local measurements of the electron-scale magnetic reconnections are reviewed in Sec. 6. Finally, we provide a summary and future perspectives in Sec. 7.

2 Background theory

In this section, we briefly introduce the physics framework of magnetic reconnection, mainly from the microscopic point of view. Comprehensive reviews ranging from the theoretical basis to experimental and astrophysical applications are available in the literature (Biskamp, 2000; Zweibel and Yamada, 2009; Yamada et al., 2010). There are also review papers on magnetic reconnection in solar flares (Janvier, 2017; Isobe and Shibata, 2009) and macroscopic descriptions of magnetic reconnection (Pontin and Priest, 2022; Loureiro and Uzdensky, 2016). Ji et al. (2020) has summarized the major scientific challenges to magnetic reconnection research.
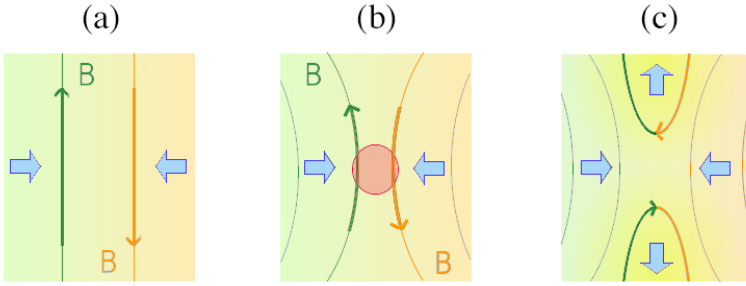
Fig. 1 A schematic picture of magnetic reconnection. (a) Approaching anti-parallel field lines (green and orange), (b) the topology of the magnetic field lines is violated in the contact region (red), and (c) the relaxation of the magnetic field configuration after the reconnection of the field lines.

2.1 A basic description of magnetic reconnection

Magnetic reconnection is a relaxation process of magnetized plasmas involving anti-parallel magnetic field components. Figure 1 shows a typical case with anti-parallel magnetic field lines. There is a magnetically null region between the anti-parallel magnetic field lines [Fig. 1 (a)]. This region is called the neutral sheet. This configuration can be disturbed by external plasma flows or internal instabilities around the neutral sheet. Once some magnetic diffusion processes violate the topology of magnetic field lines [Fig. 1 (b)], the field line structure relaxes to a more stable magnetic field configuration [Fig. 1 (c)]. This relaxation process is accompanied by an energy conversion from the magnetic field to the plasma.

The magnetic induction equation describes the global dynamics of magnetic field lines,

$$\frac{\partial}{\partial t}\mathbf{B} = \nabla \times (\mathbf{u} \times \mathbf{B}) + \nu\nabla^2\mathbf{B}, \tag{1}$$

where $\mathbf{u}$, $\mathbf{B}$, and ν are the plasma flow velocity, magnetic field, and magnetic diffusivity, respectively. The convection and diffusion terms are compared by using the magnetic Reynolds number R_m,

$$\frac{|\nabla \times (\mathbf{u} \times \mathbf{B})|}{|\nu\nabla^2\mathbf{B}|} \sim \frac{4\pi u L}{c^2 \eta} \equiv R_m, \tag{2}$$

where $\eta = (4\pi/c^2)\nu$ and L are the resistivity and scale length of the dynamics, respectively. The induction equation is equivalent to Ohm's law,

$$\mathbf{E} + \mathbf{u} \times \mathbf{B} = \eta\mathbf{J} \equiv \mathbf{R}, \tag{3}$$

where $\mathbf{E}$ and $\mathbf{J}$ are the electric field and current density, respectively. The right-hand-side term, called the non-ideal term $\mathbf{R}$, comes from the magnetic
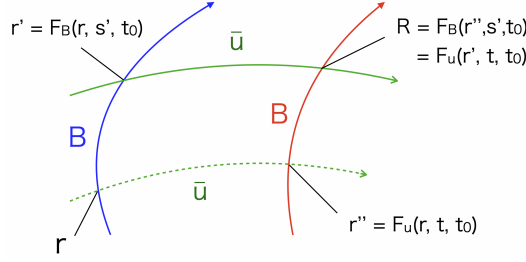
Fig. 2 The relationship between a magnetic field line, the generating functions F_B, F_u and the streaming function $\bar{\mathbf{u}}$. The blue and red lines denote the magnetic field line at times t_0 and t, respectively. The dashed and solid green lines stand for the streaming functions from the positions r and $r' = F_B(r, s', t_0)$, respectively. If the topology of the magnetic field line is conserved, a position R on the magnetic field line at t is correlated with a position r at t_0 through the two transit positions, r' and $r'' = F_u(r, t, t_0)$.

diffusion term in the induction equation. For a large Reynolds number, the induction equation and Ohm's law become

$$\frac{\partial}{\partial t}\mathbf{B} = \nabla \times (\mathbf{u} \times \mathbf{B}), \quad \mathbf{E} + \mathbf{u} \times \mathbf{B} = 0. \tag{4}$$

These equations describe ideal plasma dynamics without magnetic field diffusion.

The time evolution of the magnetic field topology is closely related to the induction equation and Ohm's law (Hornig and Schindler, 1996). The topology at time t is defined by a generating function $\mathbf{F}_B(\mathbf{r}, s, t)$,

$$\frac{\partial}{\partial s}\mathbf{F}_B = \mathbf{B}, \tag{5}$$

where s indicates the distance along a field line through the position $\mathbf{r} \equiv \mathbf{F}_B(\mathbf{r}, s = 0, t)$. If there exists an s' such that $\mathbf{F}_B(\mathbf{r}, s, t) = \mathbf{F}_B(\mathbf{r}', s', t)$, $\mathbf{r}$ and $\mathbf{r}'$ are on the same field line. The topology is conserved if a streaming function of the magnetic field, $\bar{\mathbf{u}}(\mathbf{r})$, is defined with a generating function $\mathbf{F}_u(\mathbf{r}, t, t_0)$,

$$\frac{\partial}{\partial t}\mathbf{F}_u = \bar{\mathbf{u}}, \tag{6}$$

where $\mathbf{F}_u(\mathbf{r}, t = t_0, t_0) \equiv \mathbf{r}$ and

$$\mathbf{F}_u(\mathbf{F}_B(\mathbf{r}, s', t_0), t, t_0) = \mathbf{F}_B(\mathbf{F}_u(\mathbf{r}, t, t_0), s', t), \tag{7}$$

for arbitrary s, t, and $s' = s'(s, t)$, as shown in Fig. 2. This condition can be represented in a differential form,

$$\partial_s \partial_t \mathbf{F}_u(\mathbf{F}_B) = \partial_t \partial_s \mathbf{F}_B(\mathbf{F}_u). \tag{8}$$

Since $\partial_s \partial_t \mathbf{F}_u(\mathbf{F}_B) = \partial_s \bar{\mathbf{u}}(\mathbf{F}_B)$ and $\partial_t \partial_s \mathbf{F}_B(\mathbf{F}_u) = \partial_t(\mathbf{B}(\mathbf{F}_u)\partial_s s')$, we obtain

$$\mathbf{B} \cdot \nabla \bar{\mathbf{u}} = \frac{\partial}{\partial t}\mathbf{B} + \bar{\mathbf{u}} \cdot \nabla \mathbf{B} + \mathbf{B}\frac{\partial}{\partial t}\frac{\partial}{\partial s}s', \tag{9}$$

which is written in forms relevant to the induction equation and Ohm's law as

$$\frac{\partial}{\partial t}\mathbf{B} - \nabla \times (\bar{\mathbf{u}} \times \mathbf{B}) = (\sigma - \nabla \cdot \bar{\mathbf{u}})\mathbf{B}, \tag{10}$$

$$\mathbf{E} + \bar{\mathbf{u}} \times \mathbf{B} = \mathbf{S}, \tag{11}$$

where $\sigma = \partial_t \partial_s s'$ and $\mathbf{S}$ is a vector function with $\nabla \times \mathbf{S} = (\sigma - \nabla \cdot \bar{\mathbf{u}})\mathbf{B}$. The magnetic topology is conserved if we can find a streaming function $\bar{\mathbf{u}}$ and a scalar function σ to satisfy the above conditions. This is always satisfied under the ideal condition $\mathbf{S} = 0$ once $\sigma = \nabla \cdot \bar{\mathbf{u}}$, where $\bar{\mathbf{u}}$ is now equivalent to the plasma flow velocity $\mathbf{u}$. The ideal condition is sufficient for the conservation of the magnetic field topology and the non-ideal effects can potentially change the magnetic field topology.

The magnetic field topology characterizes the collisionless plasma dynamics. Magnetic field lines globally separate plasmas and inhibit plasma mixing across them. Conversely, plasma can move along magnetic field lines. Magnetic field diffusion triggers magnetic reconnection and reconstructs the magnetic field topology. The magnetic field diffusion is evident for a small magnetic Reynolds number with a small scale length. Consequently, the global plasma dynamics suddenly transition through a localized process. Magnetic reconnection can mediate various plasma transport and energy transfer phenomena with global and impulsive features.

2.2 Reconnection models

We now present the basic models of magnetic reconnection (Sweet, 1958; Parker, 1957b; Petschek, 1964; Priest and Forbes, 1986). The minimal setup of the reconnection model includes a diffusion region where magnetic field lines reconnect, plasma inflow from the boundary, and plasma outflow from the diffusion region. The ideal plasma condition is satisfied away from the diffusion region so that the plasma inflow and outflow convey magnetic field lines. Figure 3 shows typical geometries of the reconnection model.

The effectiveness of magnetic reconnection, given by the reconnection rate R_{rec}, is defined as the magnetic flux flowing into the diffusion region per unit time,

$$R_{rec} \equiv \frac{\partial}{\partial t}\frac{\Phi_{rec}}{S} \sim u_{in}B_{in}, \tag{12}$$

where Φ_{rec}, u_{in}, B_{in}, and S are the reconnecting magnetic flux, plasma inflow velocity, upstream magnetic field, and entrance area of the diffusion region on the upstream side, respectively. Using Ohm's law in ideal plasmas, $\mathbf{u} \times \mathbf{B} = -\mathbf{E}$,

the reconnection rate can be related to the out-of-plane electric field on the upstream side,

$$R_{rec} \sim u_{in} B_{in} = E_{rec}. \tag{13}$$

From Faraday's law, the out-of-plane electric field or reconnection electric field should be uniform in quasi-steady states. Inside the diffusion region with a steep magnetic field gradient, the reconnection electric field or the reconnection rate is related to the effective resistivity in a sheet structure of out-of-plane current density,

$$E_{rec} = \eta J_\perp = \nu (\nabla \times \mathbf{B})_\perp \sim \nu B_{in}/\delta, \tag{14}$$

where δ denotes the thickness of the diffusion region in the inflow direction. The reconnection electric field is also related to the geometry of the diffusion region. The plasma inflow and outflow fluxes should be in balance with each other in the steady state,

$$u_{in} S \sim u_{out} \delta, \tag{15}$$

as shown in Fig. 3. Therefore, we obtain

$$E_{rec} \sim \frac{\delta}{S} u_{out} B_{in}. \tag{16}$$

The reconnection rate is often normalized by the magnetic field and the Alfvén speed v_A at the inflow boundary. Under this normalization, the reconnection rate is related to the inflow velocity, the aspect ratio of the diffusion region, and the magnetic field diffusion,

$$\bar{R}_{rec} \sim \bar{E}_{rec} \equiv \frac{E_{rec}}{v_A B_{in}} \sim \frac{u_{in}}{v_A} \sim \frac{\delta}{S} \frac{u_{out}}{v_A} \sim \frac{\nu}{\delta v_A}, \tag{17}$$

where $\bar{R}_{rec}$ and $\bar{E}_{rec}$ denote the normalized reconnection rate and electric field, respectively.

2.2.1 Sweet–Parker model

The Sweet–Parker model (Sweet, 1958; Parker, 1957b) assumes a weak uniform resistivity due to binary collision [Fig. 3 (a)]. The uniform resistivity triggers magnetic reconnection. The plasma outflow is supported by the magnetic tension of reconnected field lines, i.e., $u_{out} = v_A$. Theoretical analyses based on the magnetohydrodynamics (MHD) model show that the diffusion region in this model tends to elongate along the incoming magnetic field lines.
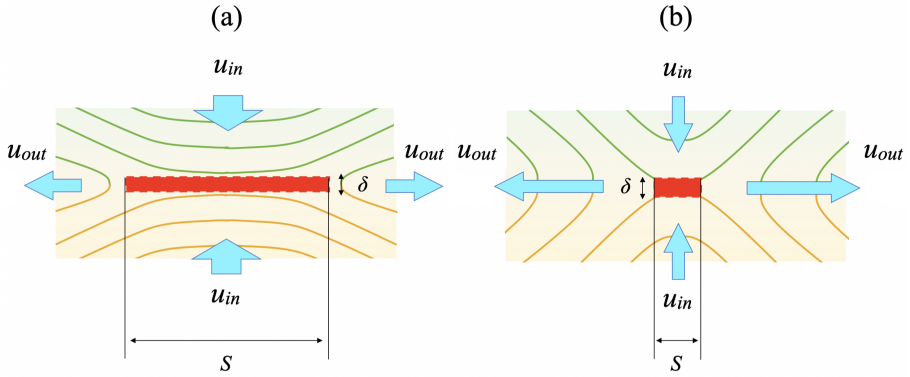
Fig. 3 Schematic pictures of classical magnetic reconnection models: (a) The Sweet–Parker model and (b) the Petcheck model. The red rectangles show the diffusion regions. The thicknesses and widths of the diffusion regions are given by δ and S, respectively. The blue arrows indicate plasma inflow to the diffusion region (vertical direction) and plasma outflow from the diffusion region (horizontal direction).

As a result, the reconnection rate decreases as the resistivity becomes small,

$$\bar{E}_{rec} = \frac{\delta}{S} \sim \sqrt{\frac{\nu}{v_A L}} \sim R_m^{-1/2}. \tag{18}$$

This model has been validated by MHD simulations and experiments employing collisional plasmas (Sato and Hayashi, 1979; Biskamp, 1986; Yamada et al., 2006). However, the expected reconnection rates are too small to explain the reconnection events observed in the solar corona, the Earth's magnetosphere, and fusion core plasmas. The time scales of magnetic reconnection can be estimated as

$$t_{rec} \sim \frac{L}{u_{in}} \sim \frac{L}{v_A} R_m^{-1/2}, \tag{19}$$

where L is the typical scale of the magnetic field configuration, and is roughly 10^8 [s] (in the solar corona), 10^4 [s] (in the magnetosphere), and 10^{-2} [s] (in a fusion core). These values are much larger than the observed time scales, for example, 10^2–10^3 [s] in coronal mass ejection and an aurora substorm, and 10^{-4} [s] in a sawtooth crash. The normalized reconnection rate required to explain these events is commonly $\bar{E}_{rec} = u_{in}/v_A \sim 0.1$. The magnetic field diffusion due to binary collision does not explain such fast magnetic reconnection. The reconnection rate problem is a starting point of magnetic reconnection research and summarized in the review paper Cassak et al. (2017).

2.2.2 Petcheck model

The Petcheck model (Petschek, 1964) is one of the alternative models used to realize larger reconnection rates [Fig. 3 (b)]. This model employs a localized

diffusion region with a small entrance area on the upstream side. The widely-opened downstream region is supported by slow mode shocks that connect to the upstream region through discontinuities. The resulting reconnection rate,

$$\bar{E}_{rec} \sim \frac{\pi}{8}\ln^{-1}(R_m),\tag{20}$$

barely depends on the Reynolds number. Therefore, this model can explain the fast magnetic reconnection in space and fusion plasmas with large Reynolds numbers. However, this model is realized in MHD simulations only when artificial resistivity models, such as

$$\eta = \eta_0(J - J_0)^{\alpha},\tag{21}$$

are employed instead of uniform resistivity due to binary collision, where α is a constant number.

2.3 Multi-scale physics in magnetic reconnection

Magnetic reconnection connects two different regimes in the physics hierarchy. The first is internal and local physics inside the diffusion region. As indicated in the reconnection models, fast magnetic reconnection may require microscopic mechanisms beyond binary collisions. The second is the external and global physics around the reconnection region, such as magnetospheric convection (Lui, 2000; Mozer et al., 2003), flux rope formation in the solar corona (Chen, 2011; Cheng et al., 2003), internal kink mode activities in torus plasmas (Chapman et al., 2010), and reformation of the magnetic configuration during spheromak merging (Ono et al., 1997). The reconnection rate in Eq. 17 is given by external physics (u_{in}), internal physics (η), and their connection (δ/S). This implies that these regimes of physics are closely related and all potentially contribute to the reconnection process.

Magnetic reconnection is a multi-scale process, which makes a complete understanding of magnetic reconnection challenging. Global MHD simulations can be used to demonstrate macroscopic plasma phenomena with an empirical resistivity model (Nishizuka et al., 2008). First-principles models, such as fully kinetic particle-in-cell (PIC) simulations (Birdsall and Langdon, 1991), can address non-ideal effects but only in a limited region near the reconnection region because of computational limitations. Mesoscopic models, such as hybrid PIC (Karimabadi, 2004), gyrokinetic (Muñoz et al., 2015), and implicit kinetic (Ricci et al., 2002) models, and the multi-hierarchy model (Usami et al., 2013) may be helpful in providing a more complete picture of magnetic reconnection under dynamical interactions between macro- and microscopic plasma dynamics.

Similarly, solar observation satellites provide global images of macroscopic plasma dynamics (Tsuneta et al., 2009), while in-situ satellite observations in the Earth's magnetosphere can measure detailed plasma environments in the vicinity of the reconnection region (Sergeev et al., 1995; Burch et al.,

2016; Borg et al., 2005; Contel et al., 2006; Runov et al., 2006). Experimental studies are a powerful approach to this issue because various imaging and local measurement techniques can be employed simultaneously for carefully resized magnetic reconnection phenomena.

2.4 A microscopic description of magnetic reconnection

Using the two-fluid description, we now discuss the relationship between magnetic reconnection and microscopic plasma dynamics. The two-fluid equations are

$$n_s m_s (\frac{\partial}{\partial t}\mathbf{u}_s + \mathbf{u}_s \cdot \nabla \mathbf{u}_s) + \nabla \cdot \mathbf{P}_s = q_s n_s(\mathbf{E} + \mathbf{u}_s \times \mathbf{B}) + \mathbf{F}_s + \tilde{\mathbf{F}}_s, \quad (22)$$

where n_s, m_s, q_s, $\mathbf{u}_s$, and $\mathbf{P}_s$ are the number density, mass, charge, flow velocity, and pressure tensor, respectively. $\mathbf{F}_s$ and $\tilde{\mathbf{F}}_s$ are friction forces due to collision and micro-turbulences, respectively. The subscript s denotes the particle species, where $s = i$ for ions and $s = e$ for electrons. The ideal condition is

$$\mathbf{E} + \mathbf{u}_s \times \mathbf{B} = \mathbf{R}_s = 0, \quad (23)$$

where R_s represents the non-ideal terms,

$$\mathbf{R}_s \equiv \frac{m_s}{q_s}(\frac{\partial}{\partial t}\mathbf{u}_s + \mathbf{u}_s \cdot \nabla \mathbf{u}_s) + \frac{1}{q_s n_s}\nabla \cdot \mathbf{P}_s - \frac{\mathbf{F}_s + \tilde{\mathbf{F}}_s}{q_s n_s}. \quad (24)$$

The two-fluid equations are related to Ohm's law:

$$\mathbf{E} + \mathbf{u} \times \mathbf{B} = \mathbf{R} \quad (25)$$
$$\equiv \frac{m_e}{qn}(\frac{\partial}{\partial t}\mathbf{j} + \nabla \cdot (\mathbf{u}\mathbf{j} + \mathbf{j}\mathbf{u})) - \frac{1}{qn}\nabla \cdot \mathbf{P}_e - \frac{1}{qn}(\mathbf{F}_e + \tilde{\mathbf{F}}_e) - \frac{1}{qn}\mathbf{j} \times \mathbf{B},$$

where $\mathbf{u} = (m_e \mathbf{u}_e + m_i \mathbf{u}_i)/(m_e + m_i)$ and $\mathbf{j} = nq(\mathbf{u}_i - \mathbf{u}_e)$. Here we assume $m_i >> m_e$ and $q = q_i = -q_e$. The first three terms on the left-hand side originate from electron dynamics.

We consider the effects of the $\mathbf{j} \times \mathbf{B}$ and $\nabla \cdot \mathbf{P}_e$ terms on the magnetic field topology. Ohm's law with the $\mathbf{j} \times \mathbf{B}$ term, called the Hall term, is

$$\mathbf{E} + \mathbf{u} \times \mathbf{B} = -\frac{1}{qn}\mathbf{j} \times \mathbf{B} \rightarrow \mathbf{E} + \mathbf{u}_e \times \mathbf{B} = 0. \quad (26)$$

Thus the condition for conservation of the magnetic field topology in Eq. 11 is satisfied for $\bar{\mathbf{u}} = \mathbf{u}_e = \mathbf{u} - \mathbf{j}/qn$ and $\sigma = \nabla \cdot \bar{\mathbf{u}}$. This means the Hall term alone cannot disturb the topology because the electron flow convects magnetic field lines. The diagonal components of the pressure tensor $\mathbf{P}_{dia}$ satisfying $\nabla \times (\nabla \cdot \mathbf{P}_{dia}) = 0$ also do not disturb the topology. This is because the diagonal
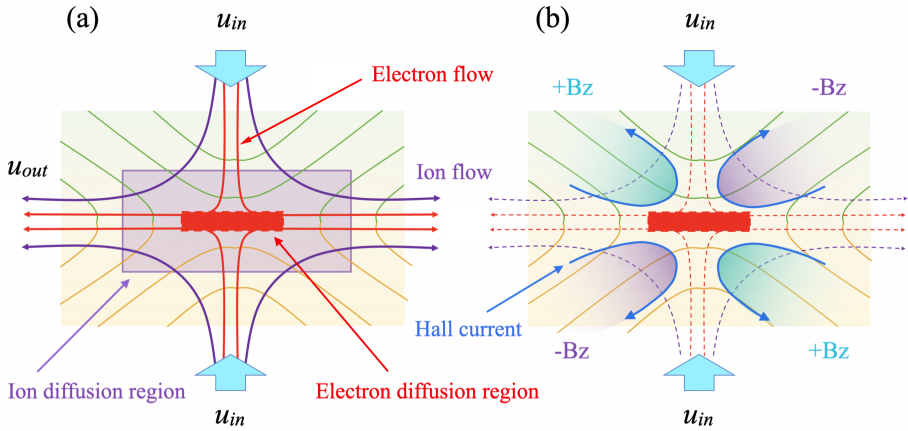
Fig. 4 Microscopic structures in the reconnection region. (a) Two-scale structures of the magnetic diffusion region. The red and purple rectangles represent the electron and the ion diffusion regions, respectively. The red and purple arrows indicate the typical electron and ion flow lines, respectively. (b) The quadrupole magnetic field (green and purple shadows) and in-plane current loops, or Hall current (blue arrow) structures resulting from the decoupling of the electron and ion flows.

component in $\mathbf{S}$ does not affect the required condition given by $\nabla \times \mathbf{S}$ in Eq. 11. On the other hand, the off-diagonal components, $\pi = \mathbf{P} - \mathbf{P}_{dia}$, of the electron pressure tensor can trigger magnetic reconnection.

The Hall term comes from the decoupling of the electron and ion flows and is evident on spatial scales smaller that the ion inertia length $d_i = c/\omega_{pi}$ or the ion gyroradius. The other terms relevant to electron non-ideal effects have characteristic scales comparable to the electron inertia length $d_e = c/\omega_{pe}$. The pressure tensor has only diagonal components for gyrotropic particle motion. Therefore, the non-diagonal component becomes evident on a spatial scale smaller than the electron gyroradius. This consideration produces the two-scale structures of the magnetic reconnection region (Hesse et al., 1999; Shay et al., 2007; Mozer, 2005) shown in Fig. 4 (a). The magnetic field lines are reconnected inside the electron diffusion region with a thickness comparable to the electron inertia length or gyroradius. The ion diffusion region, with a thickness comparable to the ion inertia length or gyroradius, surrounds the electron diffusion region.

2.5 Hall magnetic reconnection

The two-scale structure of the reconnection region has inspired a new reconnection model describing the plasma dynamics around the electron diffusion region (Drake et al., 2008; Huba and Rudakov, 2004; Rogers et al., 2001; Shay et al., 2001; Cassak et al., 2006; Biskamp et al., 1997; Yoon and Bellan, 2017). The electron diffusion region replaces the diffusion region in the Sweet–Parker model. The Hall MHD model with non-ideal ion effects governs the plasma

dynamics,

$$\mathbf{E} + \mathbf{u} \times \mathbf{B} = -\frac{1}{qn}\mathbf{j} \times \mathbf{B} + \eta_{eff}\mathbf{j}, \tag{27}$$

where effective resistivity η_{eff} represents the non-ideal electron effects dominating inside the electron diffusion region.

As explained below, this model realizes fast magnetic reconnection with a large reconnection rate. The plasma wave characterizing the plasma outflow is a whistler wave instead of an Alfvén wave. The dispersion relation derived from the collisionless Hall MHD model is

$$\omega_{\pm} = \frac{\sqrt{(kd_i)^2 + 4} \pm kd_i}{2} kv_A. \tag{28}$$

For a large spatial scale, $kd_i << 1$, the dispersion relation $\omega = kv_A$ is equivalent to that of an Alfvén wave. If the spatial scale is smaller than the ion inertia length, $kd_i >> 1$, the dispersion relation is $\omega_+ \sim k^2 d_i v_A$. In this case, the outflow flux rather than the outflow velocity is constant because

$$u_{out}\delta \sim (\omega_+/k)k^{-1} = d_i v_A, \tag{29}$$

where δ is the thickness of the electron diffusion region. The flow velocity increases as it approaches the electron diffusion region, indicating a widely-opened downstream region. The maximum outflow velocity is

$$u_{out} \sim \frac{d_i}{d_e}v_a = v_{Ae}, \tag{30}$$

for $\delta \sim d_e$, where v_{Ae} is the electron Alfvén speed. As a result, the plasma and magnetic field lines effectively flow out to realize fast magnetic reconnection. The outflow structure determines the reconnection rate independently of the trigger mechanism or the effective resistivity. Therefore, this model is applicable to active reconnection events in collisionless space plasmas.

The outflow structure is characterized by a quadrupole magnetic field and in-plane current loops, as shown in Fig. 4 (b). These originate from the decoupling of electron and ion flows. In-situ satellite observations have confirmed quadrupole structures near the reconnection region with anti-parallel magnetic fields (Mozer et al., 2002; Nagai et al., 2001; Vaivads et al., 2004). The Magnetic Reconnection eXperiment (MRX) has demonstrated fast magnetic reconnection accompanied by a quadrupole magnetic field in the collisionless regime (Yamada et al., 2006, 2018), as shown in Fig. 5 (a).

The roles of the Hall effect on fast magnetic reconnection have been examined in a comparative simulation study, the Geospace Environmental Modeling (GEM) challenge (Birn et al., 2001; Hesse et al., 2001; Ma and Bhattacharjee, 2001; Otto, 2001; Pritchett, 2001). MHD, Hall MHD, hybrid PIC, and fully kinetic PIC models were employed to simulate magnetic reconnection in
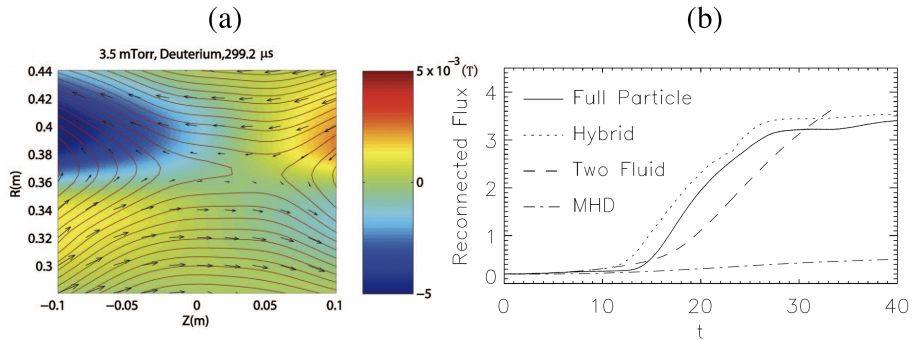
(a)   (b)

Fig. 5 (a) The magnetic field measured in the near-collision-free regime in MRX (Yamada et al., 2006). The magnetic field vectors, flux contours, and out-of-plane magnetic fields are depicted by black arrows, red lines, and colored contours, respectively. (b) The time evolution of the reconnected magnetic flux obtained from various simulation models: fully kinetic PIC, hybrid PIC, Hall MHD, and MHD (Birn et al., 2001).

a fixed magnetic field configuration. As shown in Fig. 5 (b), the reconnection rates obtained from the Hall MHD, hybrid PIC, and fully kinetic PIC models were comparable to each other and much larger than that obtained from the MHD model. This result indicates the Hall effect is needed to realize fast magnetic reconnection.

2.6 Non-ideal electron effects in the reconnection region

The non-ideal electron effects in Eq. 26 are candidate trigger mechanisms of magnetic reconnection. Among these, the anisotropic electron pressure with off-diagonal components often dominates in fully kinetic PIC simulations (Hesse et al., 2001; Ishizawa et al., 2004; Drake et al., 2009; Le et al., 2019). Long-term simulations using open boundary conditions suggest that electron dynamics inside the electron diffusion region affect plasma outflows and the reconnection rate through mesoscale structure formation (Daughton et al., 2006). The competition between the Hall effect and electron dynamics is still a subject of debate (Shay et al., 2007; Ishizawa and Horiuchi, 2005). Electron-scale dynamics are more essential in fast magnetic reconnection in electron-positron pair plasmas where the Hall effect is not effective (Ng et al., 2011; Yin et al., 2008).

Driven (or forced) magnetic reconnection models focus on the external condition as a crucial factor (Sato and Hayashi, 1979; Horiuchi and Sato, 1997; Birn, 2005; Vekstein, 2017; Pucci et al., 2018). The reconnection process reaches a quasi-steady state under the upstream boundary condition with a given out-of-plane electric field to drive the plasma inflow. Fully kinetic simulations of driven magnetic reconnection can be used to calculate the force balance in the reconnection region [Figure 6 (a)],

$$E_{rec} \sim \frac{m_e}{q_e n_e} \nabla \cdot \pi_e, \quad E_{rec} \sim \frac{m_i}{q_i n_i} \nabla \cdot \pi_i, \tag{31}$$
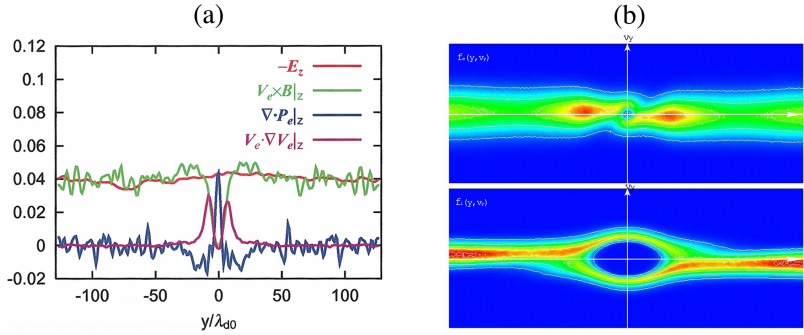
Fig. 6 (a) Spatial profiles of each term in the electron two-fluid equation resulting from a two-dimensional PIC simulation of driven magnetic reconnection (Ishizawa et al., 2004). The horizontal axis, y, denotes the direction of the magnetic field gradient, where $y = 0$ corresponds to the neutral sheet. The reconnection electric field (red) is generated by the pressure tensor term (blue). (b) The distribution functions of the electrons (top) and ions (bottom) in phase space (y, v_y) (Horiuchi and Ohtani, 2008).

to realize a steady state with a uniform reconnection electric field (Ishizawa et al., 2004; Ishizawa and Horiuchi, 2005), where π_e and π_i are the off-diagonal components of the electron and ion pressure tensors, respectively. These terms originate from the non-gyrotropic meandering particle motion near the neutral sheet (Parker, 1957a; Horiuchi and Sato, 1990). The typical scales of the ion and electron meandering motions determine the two-layered current sheet formed in the reconnection region.

Signatures of the off-diagonal components may be found in anisotropic distribution functions in velocity space. Anisotropic ion or electron distribution functions with (partially) ring-like and D-shaped components have been observed near the reconnection region in the Earth's magnetosphere (Burch et al., 2016a; Smith and Rodgers, 1991; Onsager et al., 1990; Phan et al., 2016). Theoretical and simulation studies have reproduced these distribution functions associated with effective ion heating and particle accelerations as well as the magnetic field diffusion (Shuster et al., 2014; Hesse et al., 2001; Horiuchi and Ohtani, 2008; Egedal et al., 2013; Drake et al., 2009; Usami and Horiuchi, 2022). Figure 6 (b) shows the complicated distribution functions around the reconnection region observed in a fully kinetic PIC simulation (Horiuchi and Ohtani, 2008).

2.7 Magnetic reconnection due to plasma micro-turbulence

Plasma micro-turbulence can also trigger magnetic reconnection through wave-particle resonance and anomalous magnetic field diffusion (Drake, 1981; Gary, 1980; Huba et al., 1977; Davidson and Gladd, 1975). In linear analyses, the magnetic field configuration near the reconnection region is often approximated by Harris equilibrium with an anti-parallel magnetic field and a current sheet (Harris, 1962). Possible unstable modes in this equilibrium are summarized in
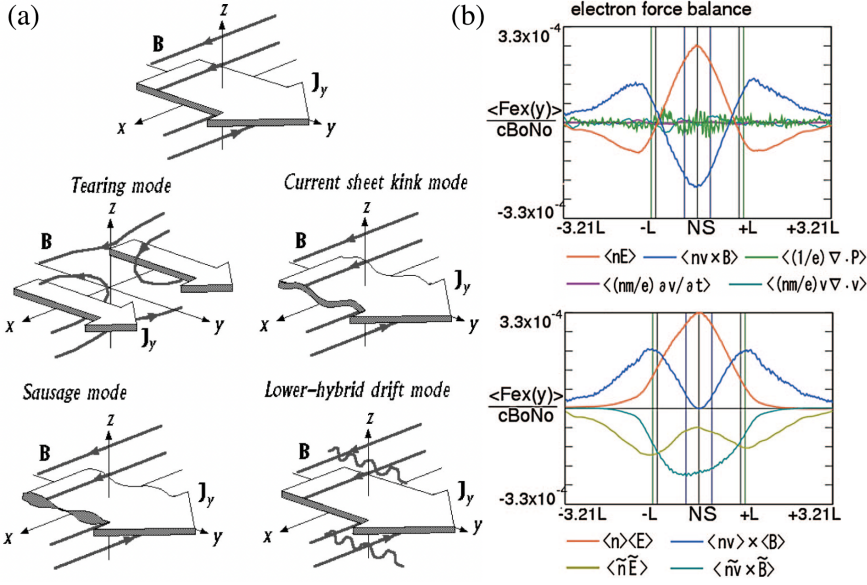
Fig. 7 (a) The configuration of an anti-parallel magnetic field and current sheet structure (top panel) and possible unstable modes (bottom four panels) (Yoon et al., 2002). (b) The spatial profiles of normalized electron force terms in the two-fluid equation (Eqs. 26 and 34) with average and fluctuation components along the current sheet. The nonlinear coupling term $\langle \tilde{n}\mathbf{v}\times\mathbf{B}\rangle$ (green line in the bottom panel) is balanced with the average electric field $\langle n\mathbf{E}\rangle$ term (red lines) at the neutral sheet (NS), indicating anomalous diffusion due to magnetic field fluctuations (Moritaka et al., 2007).

Fig. 7 (a)(Yoon et al., 2002). The tearing mode is a typical example of an unstable mode propagating along the magnetic field (Daughton and Karimabadi, 2005). The nonlinear evolution of the tearing mode dramatically modifies the diffusion region through plasmoid formation and plays a role in magnetic reconnection (Daughton et al., 2006; Pei et al., 2001; Daughton et al., 2011). On the other hand, current-driven modes propagating along the current sheet can dissipate the current density (Winske, 1981; Malkov and Sotnikov, 1981). This implies an effective resistivity η_{eff} related to the reconnection electric field,

$$E_{rec} = E_\perp \sim \eta_{eff} J_\perp. \tag{32}$$

The lower hybrid drift instability (LHDI), which occurs across a wide range of plasma conditions with steep pressure gradients, is a typical example of a current-driven mode around the reconnection region (Davidson et al., 1977; Hsia et al., 1979; Huba et al., 1980). Evidence of this instability has been identified in the Earth's magnetosphere (Huba et al., 1978; Gurnett et al., 1976). However, the LHDI is observed only in the low-plasma-beta region away from the neutral sheet in fully kinetic simulations (Silin and Büchner, 2003; Winske, 1981) and the Earth's magnetosphere (Bale et al., 2002; Shinohara et al., 1998), as indicated by nonlocal analyses (Davidson et al., 1977; Malkov and Sotnikov,

1981). MRX has also identified electrostatic fluctuations relevant to LHDI, but these are not correlated with the onset of magnetic reconnection (Carter et al., 2001). Nonlocal analyses including meandering motion (Daughton, 1999, 2002; Lapenta and Brackbill, 1997) and fully kinetic PIC simulations (Ozaki et al., 1996; Silin et al., 2005; Winske, 1981) have shown that asymmetric electromagnetic modes are unstable in the vicinity of the neutral sheet. Electromagnetic fluctuations and kinked structures in the current sheet are observed around the reconnection region in the Earth's magnetosphere (Contel et al., 2006; Runov et al., 2006; Sergeev et al., 2004). Low-frequency electromagnetic fluctuations are positively correlated with the reconnection electric field in the MRX (Ji et al., 2004; Kulsrud et al., 2005).

The effects of electrostatic and electromagnetic fluctuations due to unstable modes are incorporated into the two-fluid equations through the nonlinear coupling terms,

$$\frac{q}{m}\langle \int (\tilde{\mathbf{E}} + \mathbf{v} \times \tilde{\mathbf{B}})\frac{\partial}{\partial v}\delta f d\mathbf{v}\rangle \sim \frac{q}{m}\langle \tilde{n}\tilde{\mathbf{E}} + \tilde{n}\tilde{\mathbf{u}} \times \tilde{\mathbf{B}}\rangle, \qquad (33)$$

where the subscript ˜ and δf stand for the fluctuation component and perturbed distribution function, respectively. $\langle\rangle$ is the phase-average operator. This term may relate to the reconnection electric field,

$$E_{rec} = \langle E_\perp \rangle = -\frac{q}{n_0 m}(\langle \tilde{n}\tilde{\mathbf{E}}\rangle + \langle \tilde{n}\tilde{\mathbf{u}} \times \tilde{\mathbf{B}}\rangle + \langle \mathbf{nu}\rangle \times \langle \mathbf{B}\rangle) + \mathbf{R}_\perp, \qquad (34)$$

where $\mathbf{R}_\perp$ represents the other non-ideal terms and $\langle \mathbf{nu}\rangle \times \langle \mathbf{B}\rangle = 0$ at the neutral sheet. Two-dimensional fully kinetic simulations along the current sheet show that the longer wavelength kink mode mainly generates a perpendicular electric field (Moritaka et al., 2007), such that

$$\langle E_\perp \rangle = \eta_{eff}\langle \mathbf{J}_\perp \rangle \sim -\frac{q}{n_0 m}\langle \tilde{n}\tilde{\mathbf{u}} \times \tilde{\mathbf{B}}\rangle_\perp, \qquad (35)$$

as shown in Fig. 7 (b). This result indicates that the kink mode can trigger magnetic reconnection through anomalous diffusion. The LHDI leads to a $\langle \tilde{n}\tilde{E}\rangle$ term in the periphery of current sheet, which corresponds to the localized diffusion of the current sheet and modifies the current sheet structure (Lapenta and Brackbill, 2002; Lapenta et al., 2003). This effect does not contribute to the reconnection electric field directly but destabilizes the kink mode through modifications of the ion distribution function inside the current sheet (Moritaka and Horiuchi, 2008).

Three-dimensional considerations, including the reconnection plane, are essential to determining the roles of current-driven instabilities (Dahlburg et al., 1992; Horiuchi and Sato, 1999; Zhu and Winglee, 1996). In the case of spontaneous magnetic reconnection with open boundary conditions, the tearing instability generates flux-rope structures extending in the current sheet direction. As shown in Fig. 8 (a) and (b), the nonlinear evolution
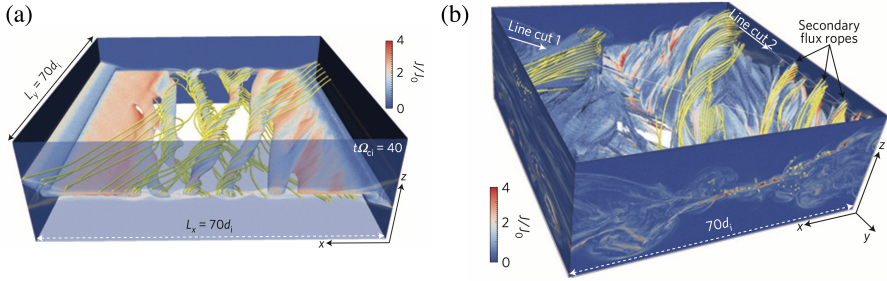
Fig. 8 Turbulent magnetic reconnection resulting from three-dimensional fully kinetic PIC simulations (Daughton et al., 2011). The three-dimensional structures are shown by density isosurfaces colored by the current density. The yellow lines indicate selected magnetic field lines. (a) The formation of primary flux ropes due to a tearing instability in the early phase. (b) The development of turbulent reconnection with secondary flux ropes in the later phase.

of the flux ropes results in a turbulent layer surrounding the reconnection region (Daughton et al., 2011; Ng et al., 2011; Chaston et al., 2009; Zhang et al., 2021), which is significantly different from the stable and isolated diffusion regions seen in conventional reconnection models. The magnetic field and current sheet profiles depart from Harris equilibrium under the plasma dynamics on the reconnection plane (Fujimoto and Sydora, 2017; Muñoz and Büchner, 2018). Linear theory and three-dimensional simulations indicate that electron shear-driven or anisotropic pressure-driven instabilities can trigger magnetic reconnection through anomalous magnetic field diffusion in such cases (Fujimoto and Sydora, 2021; Le et al., 2019; Muñoz and Büchner, 2018).

2.8 Electron diffusion region and electron-only reconnection

The electron and ion diffusion regions are also related to the energy conversion from the magnetic field, which is given by the $\mathbf{E} \cdot \mathbf{J}$ term in the energy balance equation. The energy partition is determined by the competition between electron energization near the electron diffusion region (Drake et al., 2005; Fu et al., 2006) and ion energization due to larger-scale dynamics, such as ion meandering motion and pickup process (Pei et al., 2001; Drake et al., 2009) under the Hall electromagnetic fields (Yamada et al., 2018).

High-resolution measurements are needed to explore the electron diffusion region with small spatial scales on the order of the electron inertia length, for example, 5 mm in MRX and 5-10 km in the Earth's magnetosphere (Burch et al., 2016b; Yamada et al., 2018). MRX experiments with fine structure probes and the MMS mission with cluster satellites have identified selective energy conversion for electrons in the electron diffusion region along with localized electric fields, electron exhaust jets and the crescent-shaped distribution functions (Vörös et al., 2017; Yordanova et al., 2016; Wang et al., 2017; Torbert et al., 2018; Yamada et al., 2014; Li et al., 2019). The perpendicular component, $E_\perp J_{e\perp}$, dominates in the energy conversion term in symmetric

reconnection without a guide magnetic field in MRX(Yamada et al., 2014). On the other hand, satellite observations show that large parallel electric fields in the electron diffusion region generate high-speed electron jets and $E_\parallel J_{e\parallel}$ also plays a role in the energy conversion in magnetosheath reconnection with a large guide magnetic field (Wilder et al., 2018; Wang et al., 2021).

One important result from the MMS mission is the observation of electron-only reconnection (Phan et al., 2018; Wang et al., 2021, 2018; Lu et al., 2020). In such events, only signatures of electron dynamics, such as electron heating, electron outflow, and electron-scale parallel electric field, are observed without any ion response, such as ion outflow and ion heating (Pyakurel et al., 2021). This is quite different from the standard picture of magnetic reconnection with the two-scale structure and the previous observations where ion-scale structures are primarily detected (Vörös et al., 2017; Yordanova et al., 2016; Nagai et al., 2001; Mozer et al., 2002; Phan et al., 2007). The electron-only reconnection has been observed both in the magnetosheath (Phan et al., 2018; Wang et al., 2021) and the magnetotail (Wang et al., 2018; Lu et al., 2020). The physical explanations have been presented separately for these regions.

In the magnetosheath, magnetized plasma consists of multi-scale plasma bubbles under strong turbulence. The electron-only reconnection is realized in discretized current sheets where ion response is insufficient in these small structures (Pyakurel et al., 2021; Stawarz et al., 2019; Sharma Pyakurel et al., 2019). This process could cause enhanced energy dissipation in plasma turbulence (Matthaeus and Lamkin, 1986; Sundkvist et al., 2007; Phan et al., 2018). The current sheets are also fragmented in the shock transition region. As a result, the electron-only reconnection can occur in the magnetosheath downstream of a quasi-perpendicular shock (Lu et al., 2021).

In the magnetotail without sufficient turbulence, the electron-only reconnection is considered to mediate the standard magnetic reconnection coupled with ion dynamics (Wang et al., 2020; Liu et al., 2021; Lu et al., 2022). The electron-scale thin current sheet is formed through the flux pileup in the upstream region due to external plasma flow (Lu et al., 2020) or internal instabilities (Liu et al., 2020). This process triggers the fast magnetic reconnection from a quiescent state. The resulting electron-only reconnection eventually leads to the standard reconnection. This transition originates from the flux pileup in the outflow region to regulate ion outflows (Liu et al., 2021). The Hall electric field is a main factor controlling this transition (Wang et al., 2020). The electron-only reconnection can persist sufficiently long as quasi-steady states and be detected by MMS (Wang et al., 2020).

3 Magnetic reconnection experiments with the Biermann magnetic fields generated by lasers

3.1 Laboratory astrophysics

As mentioned in Sec. 1, one of the unique features of experimental investigations of space and astrophysical phenomena is that one can control the plasma and field parameters. We are interested in applying an external magnetic field to laser-produced plasmas. Although there is always the Biermann magnetic field discussed below, we want to control the magnetic field strength and orientation using external resources. When our projects relevant to external magnetic fields were initiated in 2010, on topics such as jet propagation in an ambient magnetic field (Nishio, K. et al., 2013), magnetic field amplification via the Richtmyer–Meshkov instability (Kuramitsu et al., 2011; Kuramitsu et al., 2016), and spherical magnetized collisionless shocks (Kuramitsu et al., 2016), there were few options for producing external magnetic fields. In the early days of laboratory astrophysics, there were coil targets and pulse-power systems (Woolsey et al., 2001; Courtois et al., 2004). However, when applying a strong enough magnetic field to magnetize both ions and electrons, the space where the magnetic field was applied was too small or the capacitor bank was too large to ship abroad. Very recently, we have realized unique features of magnetized collisionless shocks in well-characterized upstream magnetized plasmas with the Gekko XII laser facility (Yamazaki et al., 2022; Matsukiyo et al., 2022). In the past, while conducting experiments with the Vulcan and LULI laser facilities, which are equipped with pulse-power systems, we carried out experiments with permanent magnets acting as external magnetic fields. Although such a magnetic field is strong enough to magnetize electrons but too weak to magnetize ions, the electrons and ions are connected by the electric and magnetic fields that they generate themselves. We expected to be able to explore something new in laboratories by controlling the external magnetic field, such as magnetic reconnection on the electron scale as discussed in Sec. 2. Before getting into our electron scale magnetic reconnection experiment, we briefly review the spontaneous magnetic field due to the Biermann battery effect below, and plasma propagation experiments in the presence of external magnetic fields in the following sections.

3.2 Biermann magnetic fields in laser-produced plasmas

It has been known since the 1970s that a spontaneous kilogauss magnetic field is generated when a solid target is irradiated with a laser (Stamper et al., 1971). Using Faraday rotation measurements, a megagauss or 100-T magnetic field was reported in a laser-produced plasma near the focal spot of a high-power laser due to the thermal baroclinic effect or the Biermann battery effect (Stamper and Ripin, 1975). More details can be found in a review on spontaneous magnetic fields in laser-produced plasmas (Stamper, 1991). Figure 9 (a)
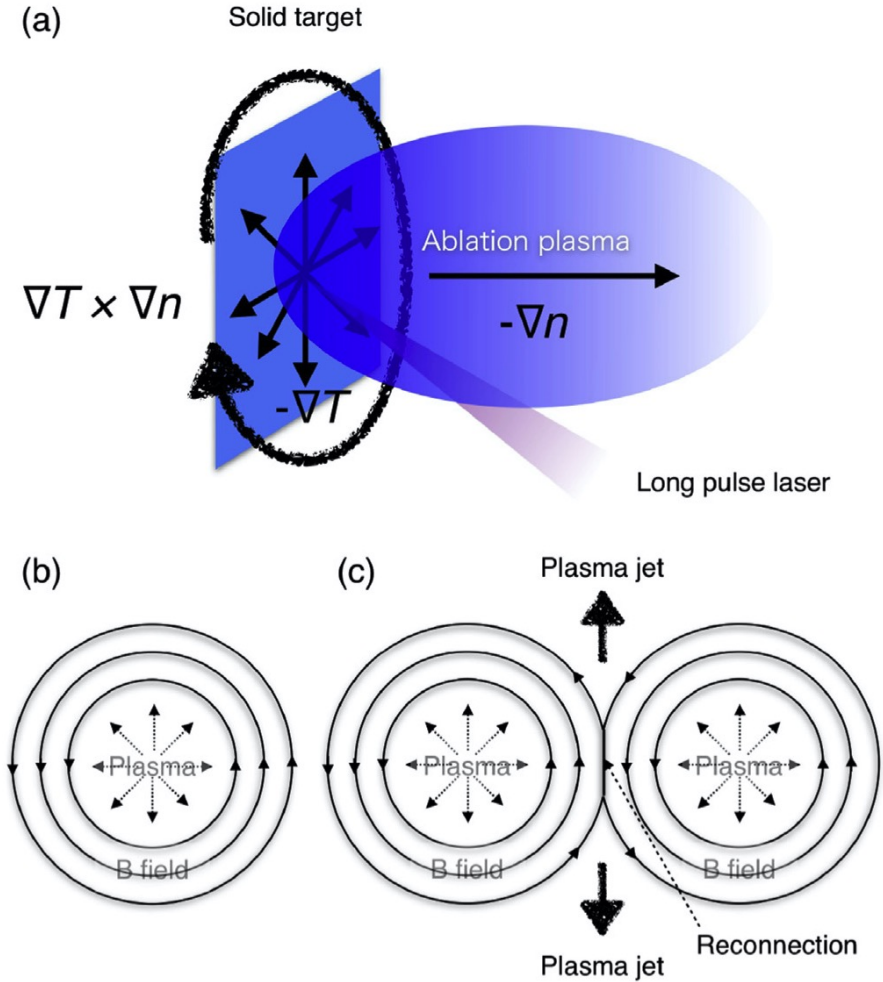
Fig. 9 (a) A schematic diagram of magnetic field generation via the Biermann battery effect. (b) The front view of the Biermann magnetic field. (c) When there are two laser beams with focal spot displacement, two magnetic bubbles are produced and magnetic reconnection can take place (Kuramitsu et al., 2015).

shows a schematic diagram of the Biermann battery effect. When a solid target is irradiated by a laser in a vacuum, an ablation plasma expands mainly in the direction normal to the target surface. The electron density gradient (∇n_e) is also in this direction, while the temperature gradient (∇T_e) is mainly along the target surface because the plasma expands in the vacuum. The Biermann battery effect arises from the null magnetic field when there is a finite angle between ∇n_e and ∇T_e. The Biermann magnetic field is proportional to $\nabla n_e \times \nabla T_e$, resulting in the formation of a magnetic bubble as shown in Fig. 9 (b). When there are two or more laser pulses focused on different
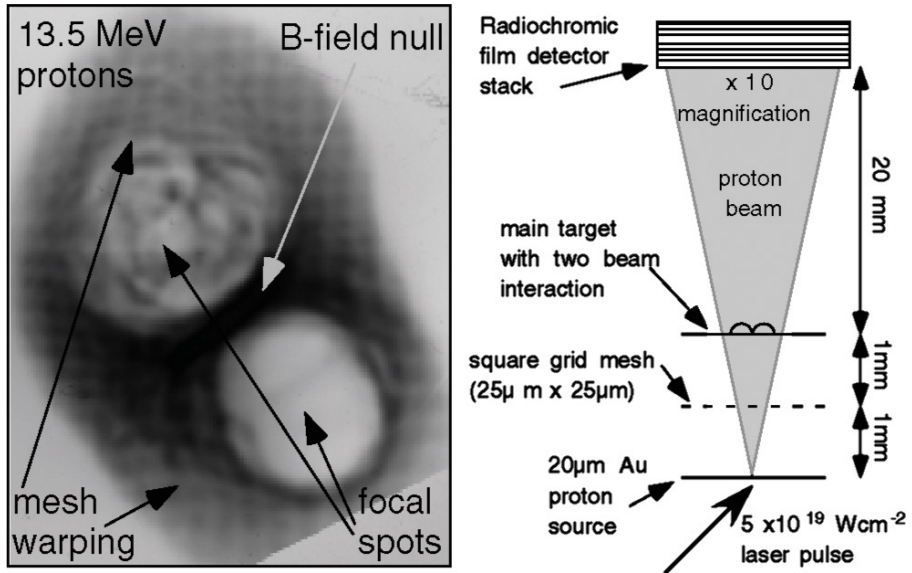
Fig. 10 Proton deflectometry showing two magnetic bubbles and a magnetic null line (Nilson et al., 2006). The main laser beams have a 1 ns pulse duration and 200 J of energy for each beam.

spots, as shown in Fig. 9 (c), magnetic reconnection takes place where the two magnetic bubbles collide.

A Biermann magnetic field is almost always generated in a laser-produced plasma, especially when a slab target is irradiated by a tight-focus laser. A massive solid target slab can maintain the bulk target material after the laser shot, and thus, the temperature gradient along the target surface. A tight-focus laser can enhance the spatial inhomogeneity $\sim \nabla$. As also discussed in the next section, one can suppress the Biermann magnetic field by irradiating a thinner target with a loose-focus laser. Even so, there must be a relatively strong Biermann magnetic field around the laser spot and laser timing. When an external field is applied, attention must be paid to the competition between the external and Biermann magnetic fields.

3.3 Magnetic reconnection with Biermann magnetic fields

We now briefly review magnetic reconnection experiments using Biermann magnetic fields. As mentioned above, most laser experiments on magnetic reconnections apply this method, which is shown schematically in Fig. 9 (c). There is an excellent review focusing on this method (Zhong et al., 2018). The experimental geometries by irradiating a slab target with two or more laser beams forming two or more magnetic bubbles have appeared in (Yates et al., 1982), where they focused on the energy deposition relevant to magnetic null points. This is now understood as the energy conversion due to magnetic

reconnections. Nilson et al. (2006) revisited the experimental geometry paying special attention to magnetic reconnection using the Biermann magnetic field. This opened up a recent trend of experimental investigations on magnetic reconnections together with the rise of laboratory astrophysics (Takabe and Kuramitsu, 2021), such as model experiments of loof-top X-ray relevant to solar flares (Zhong et al., 2010), magnetotail reconnections (Dong et al., 2012), and turbulent reconnections (Ping et al., 2023). Another important trend is magnetic reconnection experiments with capacitor coil targets, which can produce strong magnetic fields decoupled from laser plasmas (Chien et al., 2023). Here we present a typical Biermann magnetic field reconnection experiment in a laser-produced plasma.

Figure 10 shows the experimental demonstration of a laser-driven magnetic reconnection with the Biermann magnetic field (Nilson et al., 2006). The right panel shows the setup of the experiment, including proton radiography, where the two main laser beams are focused on the main planar target with focal spot displacement, and a proton source target is irradiated by an intense laser for proton radiography. Proton radiography or deflectometry is a standard method used to measure electric and/or magnetic fields by the resulting deflection of protons in laser-produced plasmas. There is a comprehensive review that provides more information (Schaeffer et al., 2022). A grid mesh is placed between the main and proton targets so that the deflections in each grid cell can be measured to reconstruct the magnetic field strength. As discussed later, even in the absence of an external magnetic field, a laser-produced plasma co-exists with an electric field and a magnetic field since the electron thermal spread is much faster than that of ions. In such a simple configuration, proton deflections on the front view, such as in the left panel in Fig. 10, are considered to be magnetic field dominated (Nilson et al., 2006). The proton image on the left in Fig. 10 shows two magnetic bubbles and a null magnetic line between them.

Note that most experiments using the Biermann magnetic field focus on a relatively short time duration and small spatial domain, comparable to the laser pulse duration and focal spot size, respectively. For instance, the left panel in Fig. 10 was taken over 1 ns and the spatial scale was several hundreds of μm larger than the focal spot of 30–50 μm but comparable to the spot separation of 400 μm. The laser-generated strong ($\sim$ 100 T) Biermann magnetic field tends to weaken as the plasma expands over time. Assuming the plasma size in Nilson et al. (2006) to be 500 μm, and if it isotropically expands in 3D up to 5 mm, then the plasma volume is 10^3 times larger. If the plasma is frozen in the magnetic field, plasma density and magnetic field strength can be decrease by 10^{-3} times. By this rough estimation, the 100 T Biermann magnetic field can decrease to $\sim$ 0.1 T after plasma expansion.

3.4 Large-scale Biermann magnetic field

As discussed above, the self-generated Biermann magnetic field is intense at the time of laser irradiation and can become weaker as the plasma expands over time. As discussed later, when a thin target burned through by a laser
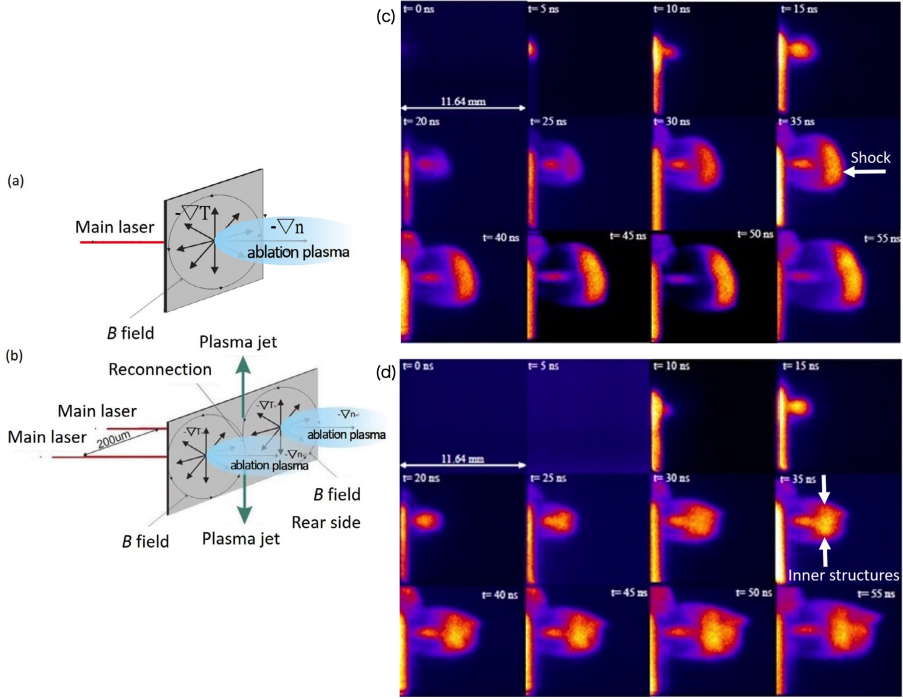
Fig. 11 Schematic laser configurations (a) with a single laser beam and (b) with two laser beams. (c) and (d) show the series of self-emission images taken by a gated 12-frame camera for (a) and (b), respectively (Khasanah et al., 2017). The main laser beams have a 0.5 ns pulse duration and an energy of 100 J per beam.

is irradiated, one can reduce the Biermann magnetic field since the target is ionized and not left behind. When we apply an external magnetic field using permanent magnets (~ 1 T on the surface at most), we do not want to have a Biermann magnetic field, and thus, we use a thin target that becomes underdense around the laser peak so that a fast rear-side plasma can be produced. Nevertheless, as shown below, the Biermann magnetic field can be essential on large spatial and temporal scales in laser-produced plasmas. Figure 11 (a) and (b) show the schematic experimental setup with a single and two laser beams, respectively (Khasanah et al., 2017). It is only when the target is irradiated by two beams with spot displacement that magnetic reconnection of the Biermann magnetic field is possible, although in this experiment, as we focus on the rear-side plasma, we expect that the thin target suppresses the Biermann magnetic field.

Figure 11 (c) and (d) show a time series of plasma propagations in an ambient plasma with single- and two-laser configurations, respectively, on large spatial and temporal scales. In the single-beam case in Fig. 11 (c), the target plasma expands and a shock is formed from ~ 20 ns. The plasma and shock then propagate in time. In Fig. 11 (d), in the early time up to ~ 20 ns, there is no significant difference from the single-beam shot. However, at the later time

of ~ 25 ns, there are transverse inner structures behind the shock, as confirmed with interferometry (not shown here) in Khasanah et al. (2017). Note that the frame at $t = 5$ ns was not operative for this shot because of a technical problem. We expect that the transverse structure observed is reconnection outflow since it is not observed in the single-shot images. Assuming the transverse expansion velocity is the outflow velocity, i.e, the Alfvén velocity, one can estimate the magnetic field strength as 0.02–0.03 T and 2–3 T for the electron and ion Alfvén velocities, respectively. As discussed above, the Biermann magnetic field can be orders of magnitude weaker than, for instance, in Fig. 10, but even a weak field can still affect the plasma evolution, as seen in Fig. 11. The competition between the Biermann and external magnetic fields on large spatial and temporal scales is still an open question.

4 Laser produced plasma in the presence of an external magnetic field

4.1 Plasma expansions in the presence of an external magnetic field

Plasma expansion in the presence of an external magnetic field has been widely investigated for laser-produced plasmas. Plasma behaviors are subject to the plasma beta (β), which is the ratio between the plasma pressure and the magnetic pressure. In low-β plasmas, where the magnetic field is dominant, the plasma expansions are affected by the magnetic field (Ripin et al., 1987; Mostovych et al., 1989; Pisarczyk et al., 1994; Faenov et al., 1996; Plechaty et al., 2013). In contrast, high-β plasmas can expel the perpendicular magnetic field, resulting in the formation of magnetic cavities (Dimonte and Wiley, 1991; Vanzeeland and Gekelman, 2004). Plasmas can freely expand along the magnetic field regardless of β (Pisarczyk et al., 1994; Faenov et al., 1996; Harilal et al., 2004).

Other important conditions are the angle between the axis of plasma propagation and the magnetic field, θ_b, and whether the plasma investigated is created on the side of the laser irradiation or the rear side of the target. In the former case, the solid target can be a slab or a thick plane, and in the latter case, the target should be thin enough that the laser can penetrate (burn) through it to create fast plasmas behind the target. As discussed above, when a thick target is irradiated, the bulk of the target remains after the laser irradiation and the temperature gradient along the target surface tends to create a Biermann magnetic field. On the other hand, when a thin target is irradiated, the target on the laser focal spot has to be underdense so that the laser burns through the target to create the rear-side plasma. This can suppress the Biermann magnetic field since there is no bulk plasma left. The Bierman magnetic field tends to be stronger when the target is thick, the laser is tight-focus, and the laser intensity is high, and vice versa.
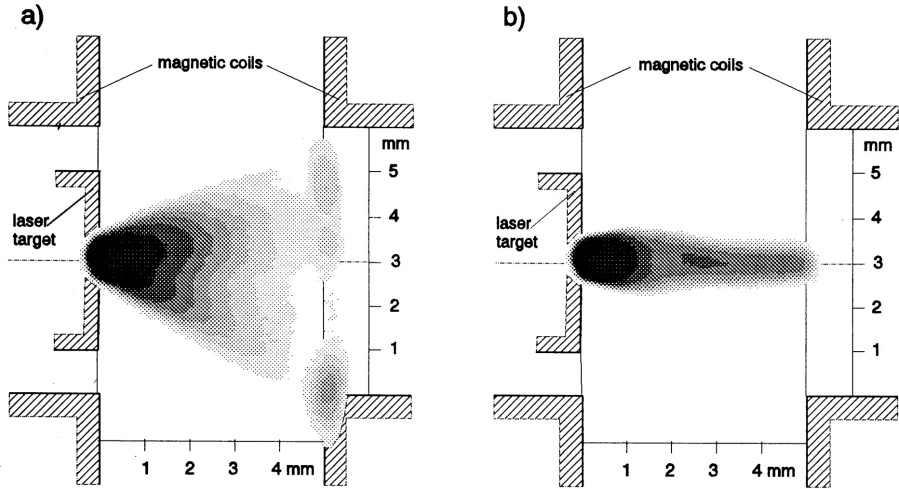
Fig. 12 Integrated soft x-ray images of plasmas (a) without $(B = 0)$ and (b) with an external, parallel magnetic field $(B = 15 - 20$ T)(Pisarczyk et al., 1994). The main laser conditions are an energy of 15 J and a pulse duration of ~ 1 ns, the target is a planar target, and the field of interest is the rear side of the target.

4.2 Parallel propagation of a low-β plasma

When a plasma propagates along an external magnetic field that is strong enough to affect the plasma dynamics, i.e., when $\theta_b = 0°$ and β is low, the plasma propagates freely along the field without expanding in the transverse direction (Pisarczyk et al., 1994; Faenov et al., 1996). Figure 12 shows integrated images of soft x-ray emissions from plasmas (a) in the absence and (b) in the presence of an external magnetic field parallel to the plasma flow. In Fig. 12 (a), the plasma expands both in the horizontal and vertical directions, and in Fig. 12 (b), the transverse plasma expansion is well suppressed by the parallel magnetic field. The kinetic pressure of the plasma is balanced with the magnetic pressure at ~ 1 mm, i.e., $\beta \sim 1$ (Pisarczyk et al., 1994).

4.3 Perpendicular propagation of a high-β plasma

High-β plasmas can expel the magnetic field (Ripin et al., 1987; Dimonte and Wiley, 1991; Vanzeeland and Gekelman, 2004), resulting in the formation of magnetic cavities. Figure 13 shows the streaked image of a magnetic field measurement by Faraday rotation (Dimonte and Wiley, 1991). The magnetic cavitation caused by plasma pressure is evident at earlier times in Fig. 13 (b) and (c). The cavitation lasts until the plasma kinetic pressure and magnetic pressure are balanced, following complicated plasma structures due to instability, as shown in Fig. 14. Figure 14 shows the time evolution of plasmas observed with a gated optical imager of plasma emission with different magnetic field strengths. When $B = 0$, the plasma expands rather isotropically as in Fig. 14 (a). When $B \neq 0$, the plasma expands, evacuating the magnetic field
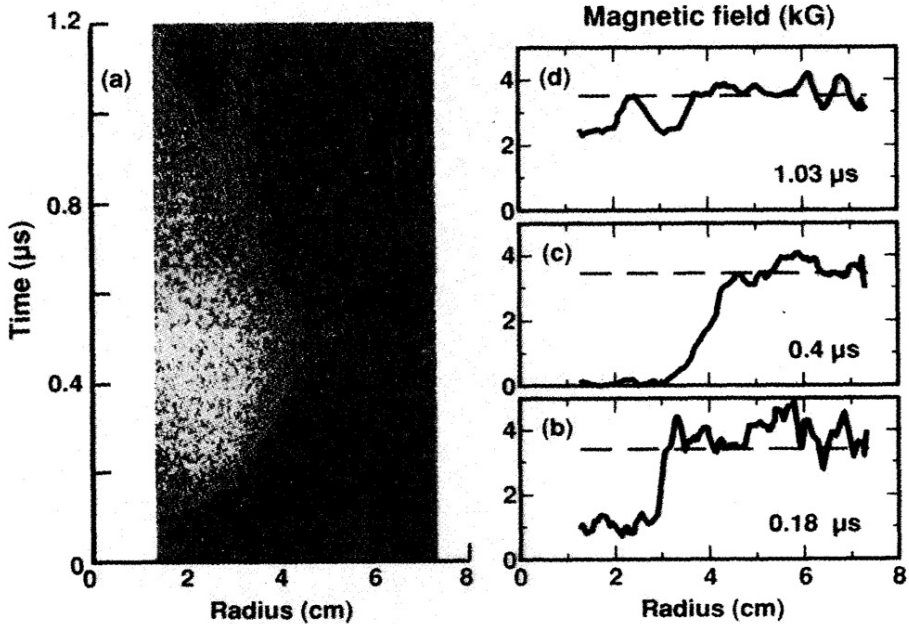
Fig. 13   (a) A streaked image of the Faraday rotation of an external probe laser in a magnetized plasma. (b)–(d) Line profiles at different times after the main laser irradiation (Dimonte and Wiley, 1991). The main laser conditions are an energy of 200 J and a pulse duration of 25 ns, with counterstreaming irradiation of a spherical target.
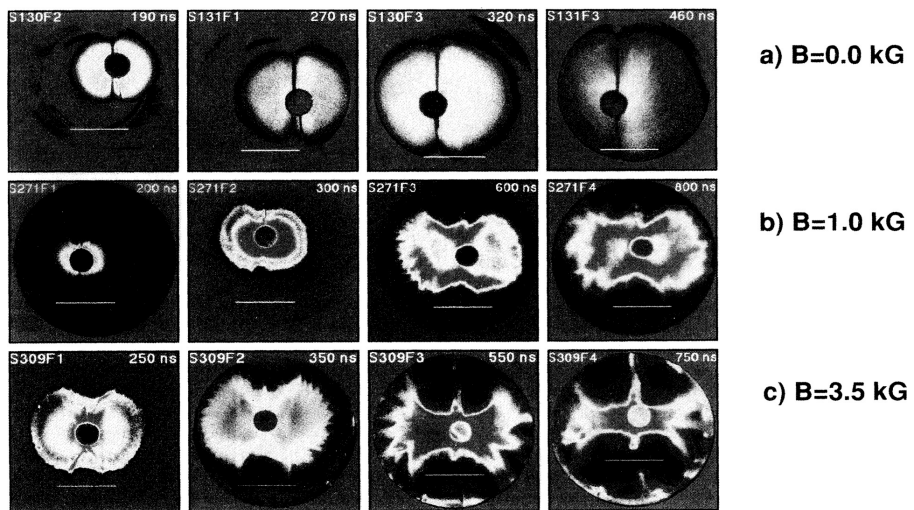

Fig. 14   Gated optical images of plasma emissions with different magnetic field strengths, (a) $B = 0$ T, (b) $B = 0.1$ T, and c) $B = 0.35$ T, pointing toward the image at different times after the main laser irradiation (Dimonte and Wiley, 1991). The laser beams come from the top and bottom of the image. The circular feature and vertical line correspond to the mask used to protect the camera from strong radiation and the scattering of the laser beams and target support, respectively.
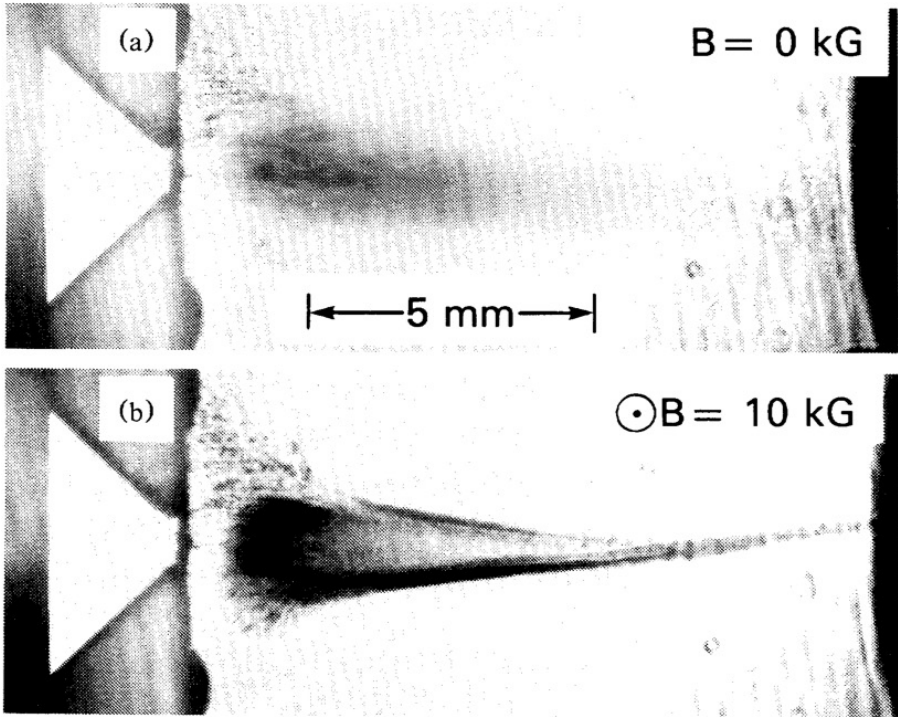
Fig. 15 Resonant absorption images with different magnetic field strengths: (a) $B = 0$ T and (b) $B = 1$ T (Mostovych et al., 1989). The main laser conditions are an energy of a few mJ and a pulse duration of 3–4 ns, the irradiated target is planar, and the field of interest is the ablation side of the target.

until $t = 350$ ns, as shown in Fig. 13. Then, the filamentary structure grows in time as in Fig. 14 (c).

4.4 Perpendicular propagation of a low-β plasma

When the magnetic field is dominant over the plasma and the field is normal to the plasma flow, so when $\theta_b = 90°$ and β is low, it is generally expected that the plasma will be decelerated and confined by the magnetic field. In the above experiments, in which the plasma kinetic energy is initially larger than the magnetic field energy, the plasma is decelerated by the magnetic field and exhibits instabilities after the expelled magnetic pressure becomes comparable to the plasma kinetic pressure (Ripin et al., 1987; Dimonte and Wiley, 1991). Even in the presence of a strong, perpendicular magnetic field, with $\theta_b = 90°$ and low β, plasma collimation and wedge formation have been observed (Mostovych et al., 1989). Figure 15 shows snapshots of plasma images (a) in the absence and (b) in the presence of a strong external perpendicular magnetic field. The effect of the external magnetic field is evident. In Fig. 15 (b), even though the plasma kinetic and thermal pressure is smaller than the magnetic field pressure, there is no evident plasma deceleration. Note
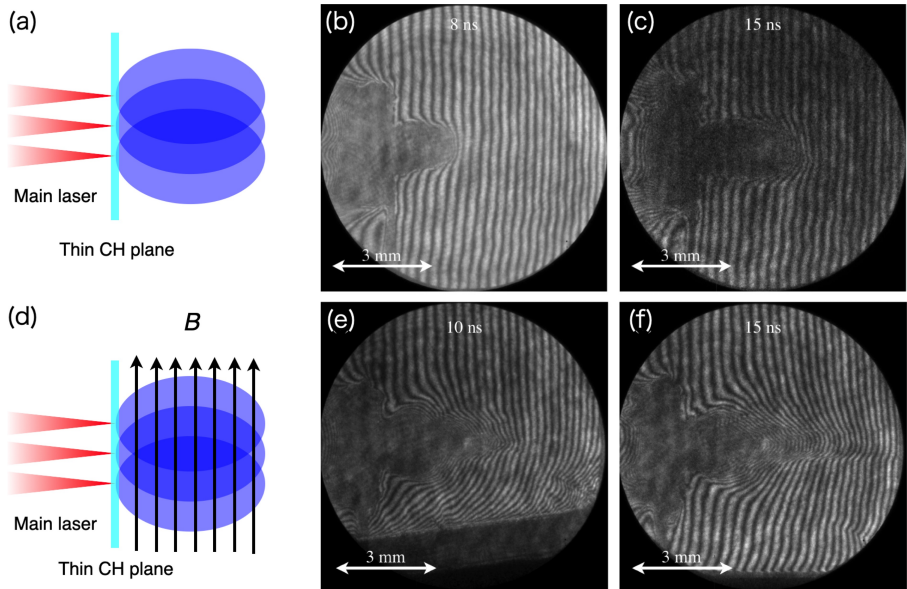
Fig. 16 (a) A schematic figure of plasma propagation in the absence of a magnetic field. Interferograms (b) at 8 ns and (c) at 15 ns from laser irradiation without an external magnetic field. (d) A schematic figure of plasma propagation in the presence of a weak magnetic field. Interferograms (e) at 10 ns and (f) at 15 ns from laser irradiation with an external magnetic field. The data are the same as in Kuramitsu et al. (2018).

that in both Figs. 14 and 15, although their β values are significantly different, the ion gyroradii are larger or comparable to the plasma scale length. However, the electrons are well magnetized, yet no discussion on the electron scale dynamics. The recent trends in experimental studies relevant to space and astrophysical phenomena have been stronger magnetic fields with pulse power (see, for example, Mabey et al., 2019) and large magnetic devices coupled with lasers (e.g., the Large Plasma Device (LAPD), Niemann et al., 2014).

5 Global imaging of magnetic reconnection driven by electron dynamics

5.1 Plasma collimation in the presence of a weak perpendicular magnetic field

We establish a simple experimental setup with and without a weak external magnetic field perpendicular to the plasma propagation direction, as shown in Fig. 16 (Kuramitsu et al., 2018). We use several Gekko XII laser beams with beam offsets to create a directional plasma jet, as shown in Fig. 16 (a) (Kuramitsu et al., 2009). In the beginning, we did not expect to observe a significant difference between the case without [Fig. 16(a)–(c)] and with [Fig. 16(d)–(f)] the magnetic field, since we applied the external magnetic field
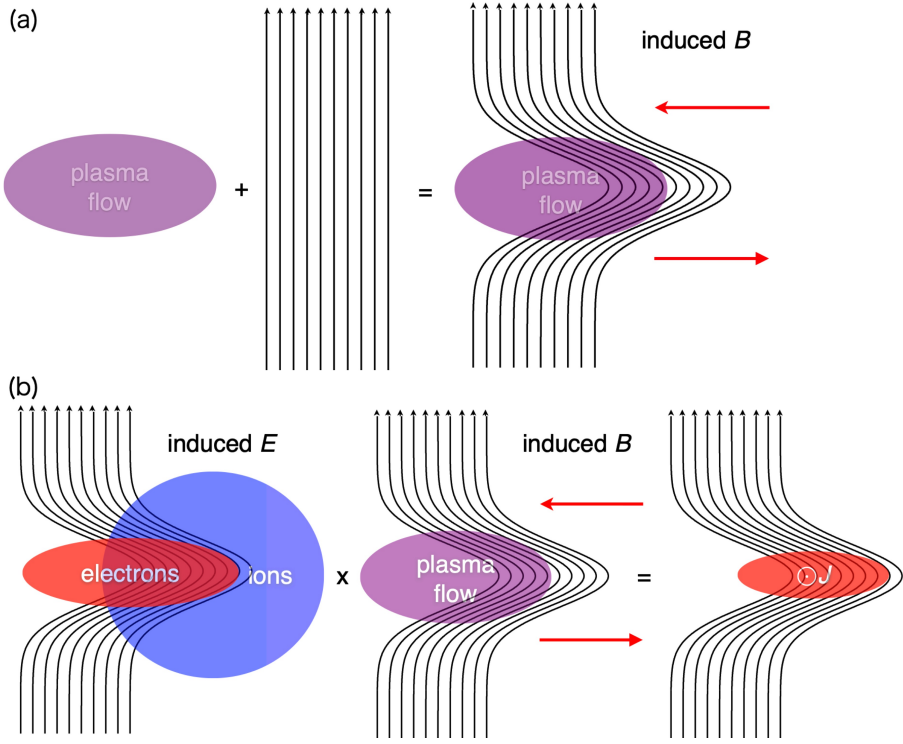
Fig. 17 (a) The plasma dynamic pressure distorts the weak magnetic field, inducing parallel and anti-parallel magnetic fields $\vec{B}$ relative to the plasma propagation direction. (b) Since the ions are not magnetized but the electrons are magnetized, the ions are ahead of the electrons, inducing a space charge and electric field $\vec{E}$. Only electrons induce the $\vec{E} \times \vec{B}$ drift and create a net current, which is consistent with the elongated anti-parallel magnetic geometry (Kuramitsu et al., 2018).

with a permanent magnet with a field strength of ~ 0.7 T at the surface and ~ 0.3 T in the plasma region. As we discuss below, the plasma kinetic energy is much larger than the magnetic field energy. However, the interferograms show clear differences between the cases with and without the magnetic field. In the presence of the external, perpendicular magnetic field, the plasma tends to collimate at large distances.

From Fig. 16 (f), it can be seen that the plasma reaches ~ 8 mm in 15 ns, and thus the plasma velocity observable from the interferometry is ~ 500 km s^{-1}. With this velocity and a magnetic field of 0.3 T, one can estimate the proton and electron gyroradii as 17 mm and 9.5 μm, respectively. Our system size is about 10 mm, and therefore, the ions are not magnetized but the electrons are well magnetized, i.e., only the electrons are directly coupled with the magnetic field.

We also define a dynamic plasma $\beta_k \sim 10^5$ using the kinetic bulk plasma energy and the magnetic field energy, with a measured plasma density. Since the dynamic or ram pressure of the plasma on the magnetic field is significantly

larger than the magnetic field pressure, the magnetic field is easily distorted. We have discussed plasma collimation with some theoretical experts in magnetohydrodynamics (MHD). It turns out that although it is possible to create a magnetic cavity due to the strong dynamic pressure, it is difficult to explain the observed plasma collimation using MHD theory. We now consider the different motions of the ions and electrons. Figure 17 schematically shows the physical consequences of this. One can see that even in the absence of a magnetic field, the plasma expands more along the axis than in the lateral direction in Fig. 16 (b) and (c). Thus, the plasma tends to push the magnetic field in this direction. This results in the induced parallel and anti-parallel magnetic fields seen in Fig. 17 (a). Furthermore, since the electrons are magnetized but the ions are not, a space charge is created, as seen in Fig. 17 (b). The induced electric field and induced magnetic field create a current, which supports the distorted anti-parallel magnetic field configuration. The current is supplied by the $\vec{E} \times \vec{B}$ drift of electrons since only the electrons are magnetized. Once the magnetic field becomes parallel to the plasma propagation direction, the electrons tend to propagate along this direction, enhancing the current and distortion. There is thus a positive feedback effect on the plasma collimation.

This scenario has been confirmed with PIC simulations (Moritaka et al., 2016; Kuramitsu et al., 2018). We perform two-dimensional (2D) PIC simulations with and without the background magnetic field by injecting plasma from the origin in the $+x$ direction. We set the injection velocity to be larger than the electron and ion thermal velocities. We set the kinetic plasma $\beta_k \sim 40$ and 4000 for electrons and ions, respectively, in the finite B case, where the external magnetic field is uniform in the $+y$ direction, perpendicular to the plasma injection direction. Further details can be found in the supplementary information of Kuramitsu et al. (2018). Figure 18 (a) and (b) show the plasma propagation in the presence and absence of the external magnetic field, respectively. The upper and lower halves show the electron density and the charge density, respectively, both in Fig. 18 (a) and (b). The magnetic field distortion and plasma collimation are clearly seen in Fig. 18 (a), but not in Fig. 18 (b). There is a positive charge ahead of the confined electrons created by unmagnetized ions. The space charge induced $\vec{E}$ field crossed with the local $\vec{B}$ field causes $\vec{E} \times \vec{B}$ drift only for the magnetized electrons, i.e., it generates a net current that induces the magnetic field, as seen in Fig. 18. Superposing this field with the background uniform magnetic field results in a distorted magnetic field consistent with the field in Fig. 18.

5.2 Cusps and plasmoids

The above experiment on plasma collimation was carried out under vacuum conditions in order to address the effects of the magnetic field. In order to further enhance the plasma collimation, and thus, to thin the current sheet, we add an ambient plasma as shown in Fig. 19 (a). We fill the target chamber with nitrogen gas. The gas is ionized by strong x-rays from laser-target interactions and magnetized. Since the laser-produced plasmas we observe are
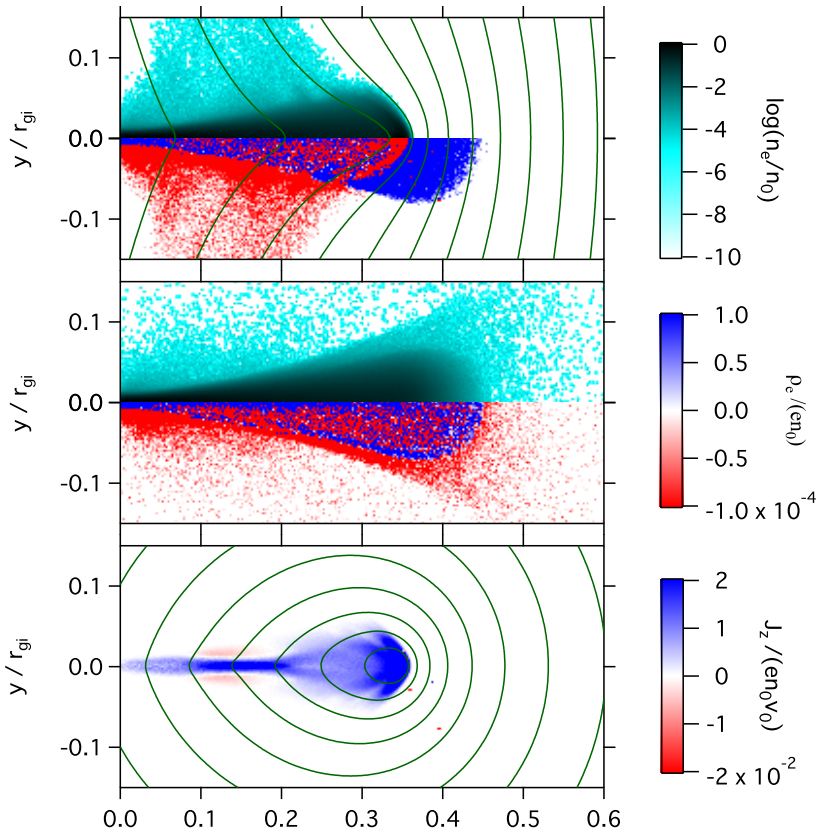
Fig. 18 (a) 2D PIC simulations of the plasma propagation under the influence of the external uniform magnetic field. The upper and lower panels show the electron density and the charge density, respectively. The solid lines show the magnetic field distorted by the plasma pressure. (b) As (a), but in the absence of an external magnetic field. (c) The current density and the current-induced magnetic field. The same parameters were used as in the runs in Kuramitsu et al. (2018).

normally supersonic, there will be a shock wave in the ambient plasma. The shocked plasma further provides external pressure to the anti-parallel magnetic field structure. Figure 19 (b) shows the self-emission image obtained with a fast-gated CCD camera, clearly showing the unique features of magnetic reconnection, that is, a cusp and plasmoid. In the early stages of the electron-scale magnetic reconnection project, we consulted solar physicists working on magnetic reconnections about how magnetic reconnections are recognized in their observations (remote images of solar plasmas) and confirmed that cusps and plasmoids are used. In the solar plasma, a flux tube can be elongated and distorted, and eventually reconnected and cut. One part comes back to the Sun and the other propagates into open space as a plasmoid. This is common in
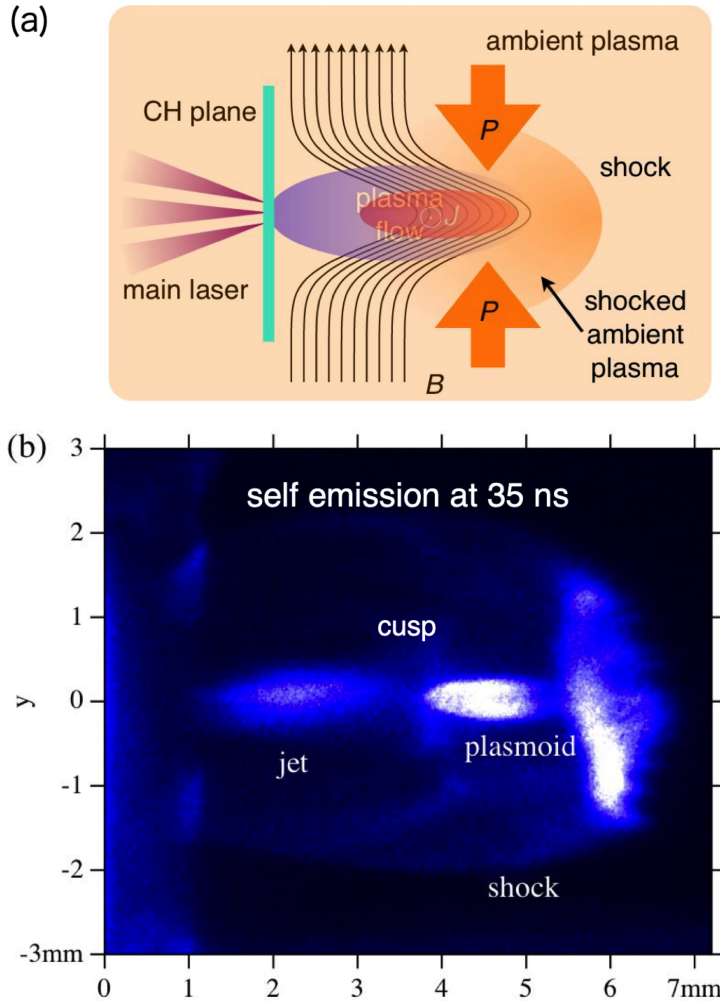
(a)

(b)

Fig. 19 (a) A schematic diagram of the experimental setup with ambient plasmas filling the target chamber with gas. The gas around the target is ionized by strong radiation from laser-matter interactions. (b) A self-emission image taken by a gated camera 35 ns from the point of laser irradiation (Kuramitsu et al., 2018).

the magnetotail reconnections in the Earth's magnetosphere, where one part coming toward the Earth becomes the origin of the aurorae, and the other propagates into open space as a plasmoid.

5.3 Electron Alfvénic outflow

The cusp and plasmoid are unique features that can be used to identify magnetic reconnection in solar plasmas. Another important feature of magnetic reconnection is an outflow propagating at the Alfvén speed. As also reported for the MMS electron-scale observations (Torbert et al., 2018), the outflow on
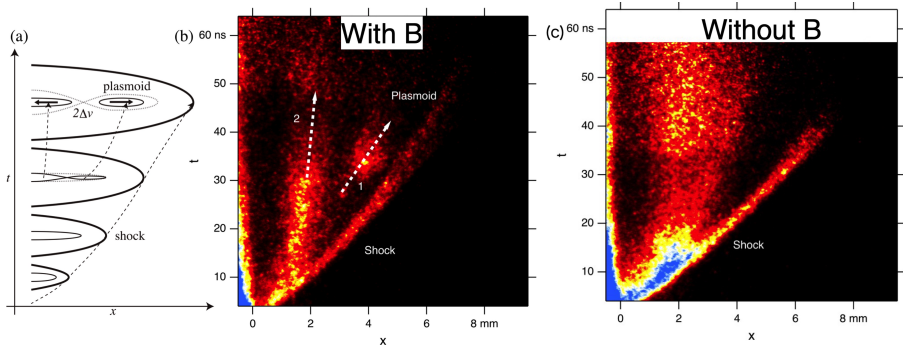
Fig. 20 (a) A schematic image of the spatiotemporal evolution of the magnetic reconnection. (b) A streaked self-emission image in the presence of the external magnetic field (Kuramitsu et al., 2018). (c) As (b), but in the absence of a magnetic field.

the electron scale propagates at the Alfvén speed defined by the electron mass. In our experiment, since only the electrons are directly coupled with the magnetic field, the inertia of the magnetic field perturbations is provided by the electrons. Figure 20 shows the spatiotemporal evolution of the magnetic reconnection driven by the electron dynamics as obtained with a streak camera. As shown in Fig. 20 (a), once the elongated magnetic field is reconnected, one can measure the separation velocity from the streaked image. First of all, in the presence of the external magnetic field [Fig. 20 (b)], a bright feature corresponding to the plasmoid is observed in the snapshot in Fig. 19 (b). In contrast, in the absence of a magnetic field [Fig. 20 (c)], there is no such feature. These observations clearly show that plasma separation occurs only in the presence of the external magnetic field. The separation velocity indicated by the white arrows is $2\Delta v \sim 100$ km s^{-1}. The Alfvén speed estimated using the electron mass, measured density, and applied magnetic field is $40 - 63$ km s^{-1}, which is consistent with the separation velocity. Our observations strongly indicate magnetic reconnection driven by electron dynamics.

6 Local measurements of magnetic reconnection in electron scale

So far, we have observed global images of plasmas. Emission images and interferograms, e.g., the images shown in Sec. 5, show structures in the electron density. However, people tend to recognize these as plasma structures because the electron motion is coupled with massive ions. It is difficult to separate electron and ion structures solely from such images. Thus, we perform local observations that can distinguish between electron and ion motions.

Since magnetic reconnection is a multi-scale process, in which the global magnetic topology changes as a result of local current dissipation, it is important to measure local quantities together with the global distributions of the
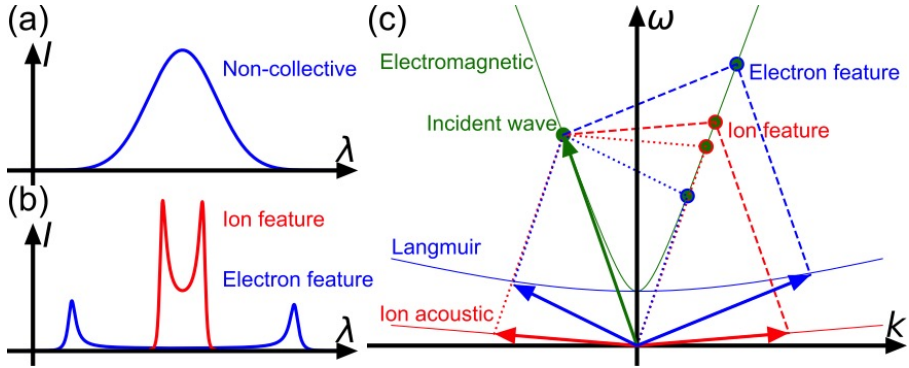
Fig. 21 Typical spectra of (a) non-collective and (b) collective Thomson scattering. (c) Parametric resonance in CTS.

plasma and magnetic field. Local observations of magnetic reconnections provide insights into the microphysics of reconnection, e.g., electron dynamics, plasma waves, and microinstabilities. In laboratory plasmas, such as laser-produced plasmas, Thomson scattering measurements (Froula et al., 2011) and magnetic induction probe measurements (Everson et al., 2009) are used for local observations.

6.1 Diagnostics

6.1.1 Thomson scattering measurements

The local distribution functions of electrons and ions can be measured using Thomson scattering, which is light scattering by charged particles, especially electrons (Froula et al., 2011). Thomson scattering is categorized as either collective or non-collective scattering in plasmas depending on the plasma parameters and diagnostic system. When the Debye length is much larger than the wavelength of the incident light, the scattering becomes non-collective, reflecting random electron motion. Figure 21 (a) shows the typical spectrum of non-collective scattering. The absolute intensity of the scattered light is proportional to the electron density. The shape of the spectrum corresponds to the electron distribution function in non-collective Thomson scattering. This can be understood as the scattered wavelength being Doppler shifted from the incident wavelength by the moving electrons. The intensity of the Doppler-shifted scattered light is proportional to the number of electrons moving at the velocity corresponding to the wavelength shift. Non-collective Thomson scattering can be adopted to measure not only Maxwellian but also arbitrary distribution functions.

On the other hand, when the Debye length is smaller than the wavelength of the incident light, the scattered light reflects collective plasma waves, which is called collective Thomson scattering (CTS). The typical spectrum (not scaled) is shown in Fig. 21 (b). CTS is a parametric resonance among incident electromagnetic, scattered electromagnetic, and plasma waves, as shown in Fig. 21
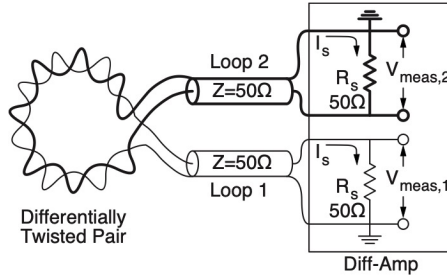
Fig. 22 A schematic circuit of the induction probe (Everson et al., 2009).

(c). The resonance with Langmuir waves corresponds to the electron feature, and that with ion acoustic waves to the ion feature. The resonant wavenumber and frequency of the plasma waves are indicated by the red and blue arrows in Fig. 21 (c). Both have two resonant peaks associated with waves propagating toward and against the observational direction or the $\vec{k}$-vector direction that is determined by the directions of the incident wave and collection optics. CTS measures the dispersion relation and the wave amplitude at the resonant wavenumber and frequency. One can estimate distribution functions from the wave properties. Assuming the distribution functions to be Maxwellian, the spectral shape of the electron feature provides the density, temperature, and velocity of the electrons, and that of the ion feature provides the temperature and velocity of the electrons and ions. Since the CTS spectrum contains information on the distribution functions, one can in principle estimate an arbitrary distribution function from the spectrum. However, the analysis for an arbitrary-shaped distribution function is complicated because the spectral shape is indirectly related to the distribution function.

6.1.2 Magnetic induction probe

The magnetic induction probe (or the so-called B-dot probe) is used to measure local magnetic fields in laboratories (Everson et al., 2009). The probe consists of loop coil(s) and measures the induction voltage relevant to the change in the magnetic field. Figure 22 shows the schematic circuit of the probe. In order to reduce noise, a pair of coils with right-handed and left-handed loops are sometimes used. When the induction occurs, the signs of the voltage of each coil are opposite. The differential amplifier allows us to measure the signal related only to the magnetic field. The integral of the measured voltage gives the absolute value of the magnetic field. Since the signal is proportional to the derivative of the magnetic field, one can find waves with frequency analysis.

6.2 Electron-only reconnection outflow

We perform an experiment focusing on local observations using CTS and the magnetic induction probe (Sakai et al., 2022). Figure 23 (a) shows the experimental setup. We employ the same method as in Sec. 5. We observe the
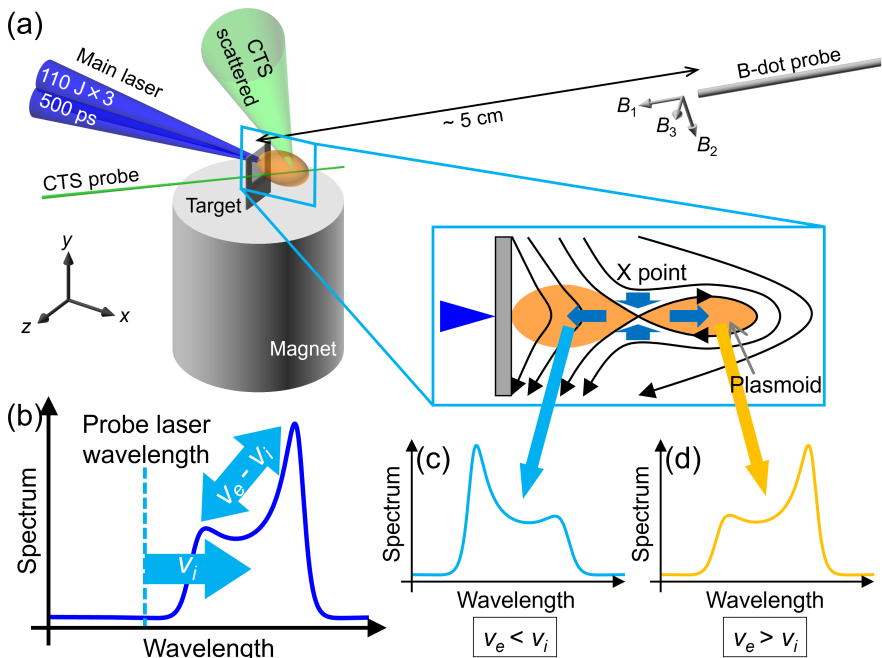
Fig. 23 (a) The experimental setup (Sakai et al., 2022). (b) A spectrum of ion feature with different electron and ion flow velocities. (c), (d) Schematic spectra on both sides of the X point.

interaction region of the magnetic reconnection with the ion feature of CTS. Figure 23 (b) shows the CTS spectrum when the electron flow velocity is different from that of the ions. The ion velocity determines the Doppler shift, i.e., the wavelength shift of the spectral center from the wavelength of the probe laser. The velocity difference between the electrons and ions affects the rate of Landau damping at the resonant phase velocities of the ion acoustic wave, i.e., the spectral asymmetry of the two peaks. If the plasmoid and cusp propagating at the electron Alfvén velocity in Figs. 19 and 20 are the electron outflow, the CTS spectrum should show the spatial change in the asymmetry near the X point — the spectrum in Fig. 23 (c) at the left side of X point because the electrons are slower than the ions, and that in Fig. 23 (d) at the right side of X point because the electrons are faster than the ions.

Figures 24 and 25 show the electron and ion velocity measurements. The experimental results in the presence and absence of the external magnetic field are compared in Fig. 24 (a)–(c) and (d)–(f), respectively. Figure 24 (a) and (d) show the self-emission images taken 50 ns after the main laser irradiation. Note that the plasmoid and cusp shown in Fig. 19 are smeared in Fig. 24 (a) because the CTS probe beam ionizes the plasma. Figure 24 (b) and (e) show the CTS images of the ion feature and the spectral profiles are plotted in Fig. 24 (c) and (f). In order to obtain the flow velocity of the electrons and ions,
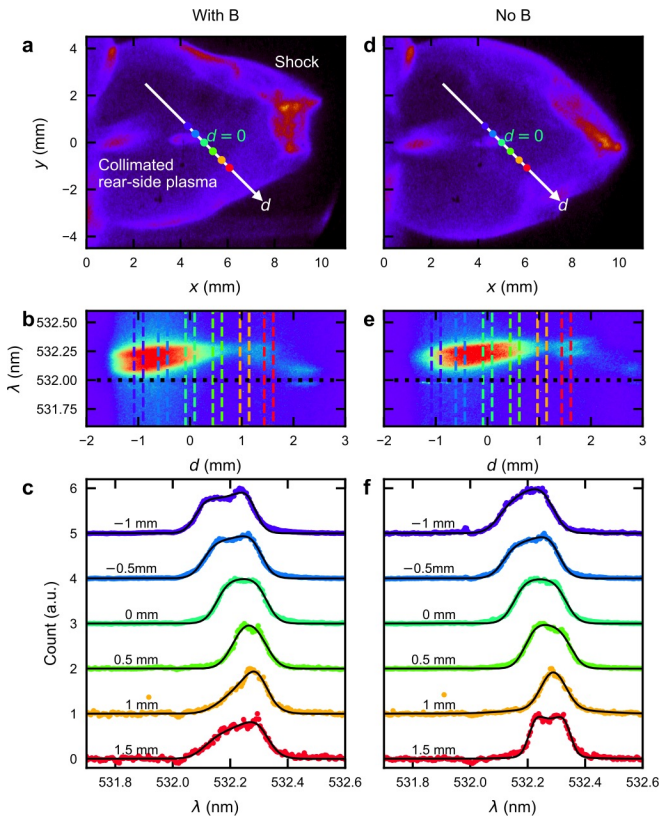
Fig. 24 Global and local observations of electron-scale magnetic reconnection (Sakai et al., 2022). (a)–(c) and (d)–(f) are the results with and without the external magnetic field. (a), (d) Self-emission images. (b), (e) CTS spectral images. (c), (f) Profiles of (b) and (e).

the profiles are fitted with the scattering form factors [black curves in Fig. 24 (c) and (f)], which represent the theoretical CTS spectrum. Figure 25 shows the spatial distribution of velocity differences with and without the external magnetic field obtained from the CTS spectra. Although the ion velocities are near constant regardless of the external magnetic field, only the electrons are exhausted from $d \sim 0$ in the presence of the external magnetic field. This is considered to be the electron outflow, as illustrated in the inset of Fig. 25. Using the electron and ion velocities, the gyroradius $[r_{gj} = m_j v_j c/(q_j B)]$ and magnetization $[\sigma_j = B^2/(4\pi n_j m_j v_j^2)]$ are $r_{ge} \sim 36$ μm and $\sigma_e \sim 0.22$ for electrons, $r_{gp} \sim 4.9$ mm and $\sigma_p \sim 8.7 \times 10^{-2}$ for protons, and $r_{gc} \sim 14$ mm and $\sigma_c \sim 1.3 \times 10^{-2}$ for carbons. Since the experiment is on the millimeter scale, only the electrons are magnetized and interact with the external magnetic field. As the difference in the electron velocity is ~ 2500 km/s, the electron outflow velocity of ~ 1200 km/s is comparable to the electron Alfvén velocity of $v_{Ae} \sim 900$ km/s. This indicates that the electrons and ions move differently
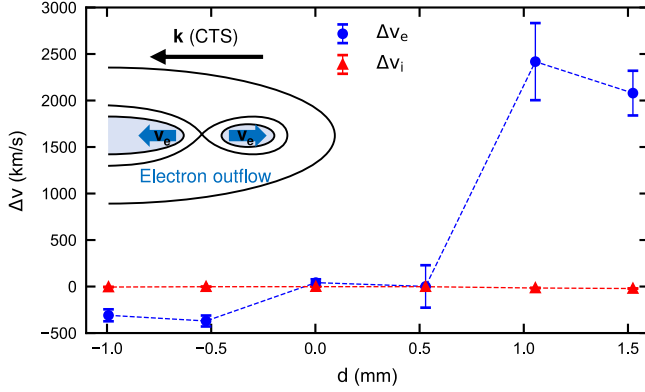
Fig. 25 Velocity difference with and without the external magnetic field (Sakai et al., 2022).

on scales less than the ion gyroradii; there are electron Alfvénic outflows but no ion outflows.

6.3 Detection of plasmoid and whistler waves

We observe the plasmoid and whistler waves associated with electron-scale magnetic reconnection using a 3-axes magnetic induction probe (Sakai et al., 2022). The probe is located ~ 5 cm from the reconnection region. When the plasmoid propagates to the probe, the sign of the magnetic field changes, as illustrated in Fig. 26 (a). This can be observed as a tripolar shape of the induction voltage in Fig. 26 (b). As discussed before, the Biermann magnetic field always exists in laser experiments. When the Biermann magnetic field simply passes through the probe, the induction voltage shows the bipolar shape in Fig. 26 (c). Figure 26 (d) and (e) show the temporal evolution of the measured voltage and magnetic field. In the presence of the external magnetic field in Fig. 26 (d), the magnetic field inversion is observed at $t \sim 400$ ns. Since the plasmoid propagation velocity is ~ 100 km/s (Kuramitsu et al., 2018), the detection timing of 400 ns is comparable to the propagation time of the plasmoid from the reconnection region to the magnetic induction probe [(5 cm)/(100 km/s) = 500 ns].

The magnetic field in Fig. 26 (c) shows the temporal oscillation embedded in the dynamic change of the magnetic field relevant to the plasmoid. In Fig. 27 (a)–(f), we perform time-frequency analysis using the wavelet transform. Comparing the three components of the magnetic field with and without the external magnetic field, one can find a ~ 10 MHz oscillation around $t \sim 400$ ns in the B_2 and B_3 components with the external magnetic field, which are nearly perpendicular to the nominal background magnetic field, as shown in Fig. 27 (g). The frequency of the oscillation is between the gyrofrequencies of the electrons (~ 8 GHz) and ions (~ 1 MHz). As the phase difference between B_2 [Fig. 27 (b)] and B_3 [Fig. 27 (c)] in Fig. 27 (h) is $\sim 90°$, the oscillation has
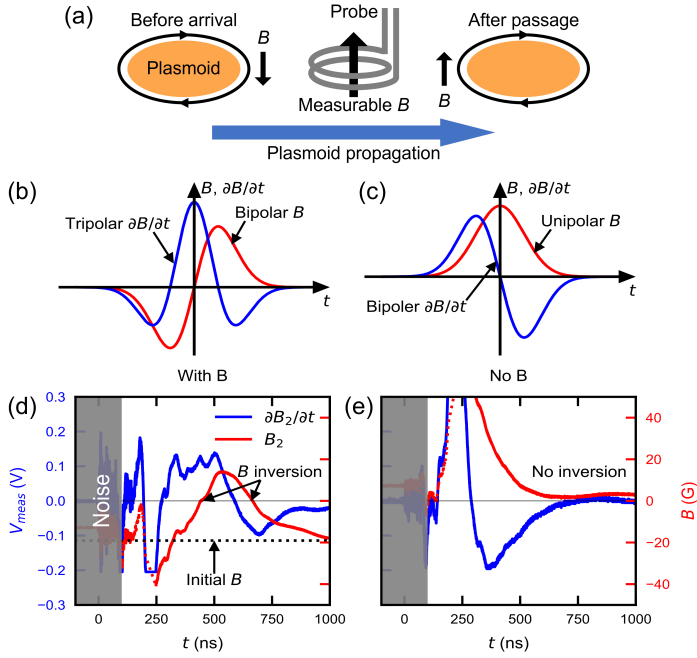
Fig. 26 Local magnetic field measurements with the induction probe (Sakai et al., 2022). (a) A schematic illustration of plasmoid propagation to the probe. (b), (c) The responses of the induction probe in the bipolar and unipolar time evolution of the magnetic field. (d), (e) The experimentally observed magnetic field.

right-hand polarization. This phenomenon is identified as whistler waves. By considering the group velocity of the whistler waves and the plasma expansion velocity from the target, the arrival time of the whistler waves at the magnetic induction probe can be estimated using the black curves in Fig. 27 (h). This is consistent with the $\sim 90°$ polarized region, so the whistler waves come from the reconnection region. The generation mechanism of the whistler waves can be a temperature anisotropy (Fujimoto and Sydora, 2008) or modified two-stream instability (Ji et al., 2004) driven by the electron outflow.

6.4 Non-Maxwellian electron distribution functions

The recent experiments with magnetic confinement devices focus on electron-scale dynamics, especially on the electron-only reconnection (Shi et al., 2022,?; Sang et al., 2022). In magnetically-confined plasmas, the spatial distribution of local density, temperature, and electromagnetic fields have been observed using multiple probes such as electrostatic and induction probes (Sang et al., 2022; Yamada et al., 2014). In the experiments by Shi et al. (2022,?), the shape of the electron distribution function downstream of the magnetic reconnection is directly measured with non-collective Thomson scattering. Figure 28 shows the electron distribution functions in the outflow direction with different positions
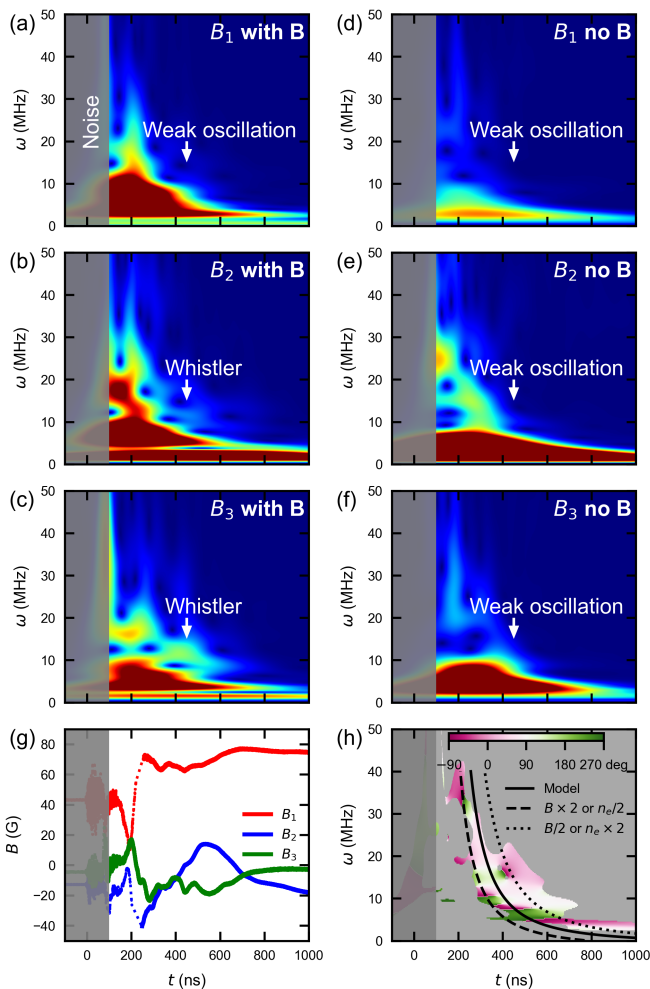
Fig. 27 Magnetic fluctuation measurements (Sakai et al., 2022). (a)–(f) Time-frequency spectrograms of three components of the magnetic field. (g) The time evolution of the magnetic field strength with the external magnetic field. (h) The phase difference between B_2 and B_3 with the external magnetic field.

and magnetic field strengths (Shi et al., 2022). The position $x = 0$ mm is the X point and Fig. 28 (a) and (b) compare the measurements on both sides of the X point with the magnetic field strength of 15 G. There are thermal electrons at rest and beam electrons moving in the outflow direction. Their Maxwellian fits are plotted as dashed curves, and the sum of two dashed ones is shown in the solid one. The electron temperatures of the thermal and beam electrons are $T_e \sim 2.8$ eV and $T_e^b \sim 0.02$ eV, respectively. The density ratio of beam electrons to thermal electrons is 0.04. The vertical dotted blue lines indicate the electron Alfvén velocity of 430 km/s and its half value. The velocity of
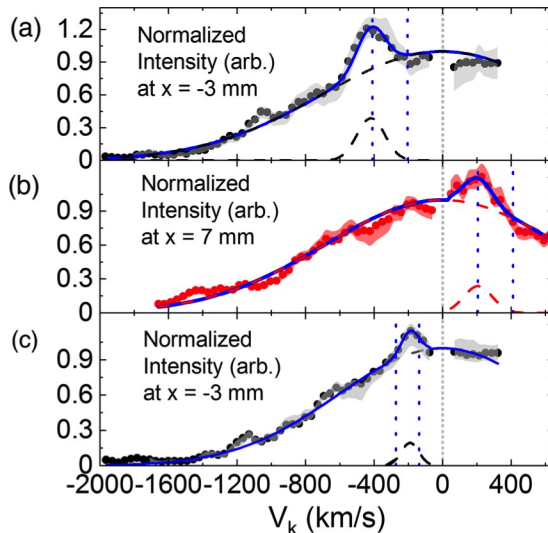
Fig. 28 Electron distribution function measurements with non-collective Thomson scattering (Shi et al., 2022). (a) $x = -3$ mm with $B_{inflow} = 15$ G. (b) $x = 7$ mm with $B_{inflow} = 15$ G. (c) $x = -3$ mm with $B_{inflow} = 10$ G. The electron Alfvén velocity is indicated by the vertical dotted blue lines.

the beam electrons is close to the electron Alfvén velocity. The beam velocity of ~ -440 km/s at $x = -3$ mm in Fig. 28 (a) and that of ~ 210 km/s at $x = 7$ mm in Fig. 28 (b) suggest the electron beams move away from the X point on both sides of the X point. Figure 28 (c) shows the scattered spectrum with the same setup as in Fig. 28 (a) but with a magnetic field strength of 10 G. The beam velocity decreases to -180 km/s as the electron Alfvén velocity does to 280 km/s. Thus, the beam component of the electron distribution function is considered to be the electron Alfvénic outflow resulting from electron-scale magnetic reconnection.

6.5 Unstable wave measurements with Thomson scattering

In electron-scale magnetic reconnection, various kinds of waves are excited as a result of microinstabilities, such as Buneman, electron two-stream, modified two-stream, and lower hybrid drift instabilities (Fujimoto, 2014). Since CTS is a parametric resonance, the dispersion property and amplitude of the excited waves can be directly observed with CTS measurements (Matsukiyo et al., 2016; Sakai et al., 2020, 2023). The CTS spectra of excited waves show large asymmetries of the electron and ion features or additional peaks associated with the waves (except for the Langmuir and ion-acoustic waves). Figure 29 shows the CTS spectrum in the presence of electron two-stream instability. The unstable distribution function is shown in Fig. 29 (a). Figure 29 (b) is the same as Fig. 21 (c) but the unstable branch is illustrated at $\omega/k \sim v_b$. This results
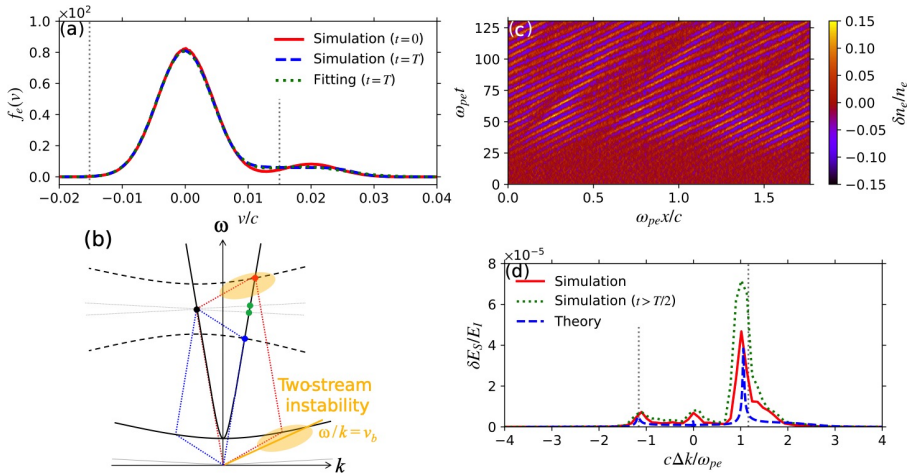
Fig. 29 A numerical simulation of the CTS spectrum in the presence of an electron two-stream instability (Sakai et al., 2020). (a) The electron distribution function. (b) A schematic illustration of the parametric resonance with the two-stream instability. (c) The spatiotemporal evolution of the density fluctuations. (d) The simulated spectrum.

in the excitation of electrostatic waves in Fig. 29 (c). The simulated spectrum in Fig. 29 (d) shows the enhancement of the right peak resulting from the instability. The intensity of the right peak is determined by the amplitude of excited waves at the resonant wavenumber and frequency. By observing spectra showing large asymmetries in electron-scale reconnection experiments, we can discuss when, where, and which type of microinstability occurs in electron-scale magnetic reconnection.

7 Summary

In this work, we have discussed magnetic reconnections driven by electron dynamics. We gave a brief review of the recent space observations of magnetic reconnections on electron scales in Section 1 and in this review, we have focused on magnetic reconnections in laser-produced plasmas, paying special attention to the electron dynamics.

In Section 2, we reviewed the classical reconnection models and the roles of microscopic plasma dynamics on magnetic reconnection. Magnetic reconnection is a multi-scale phenomenon due to the contributions of global plasma dynamics surrounding the reconnection region and local plasma dynamics inside the magnetic diffusion region. Ion-scale dynamics resulting from the decoupling between electron and ion flows potentially accelerate the reconnection process to realize fast magnetic reconnection, which can explain impulsive phenomena in collisionless space and fusion plasmas. Non-gyrotropic electron motion and interactions with micro-turbulences can violate the conservation of magnetic field topology to trigger collisionless magnetic reconnection. We

also introduced signatures of these microscopic dynamics in in-situ satellite observations and laboratory experiments.

In Section 3, we briefly reviewed magnetic field generation via the Biermann battery effect. When a solid slab target is irradiated by a laser pulse, a Biermann magnetic field is generated on the surface of the target. By using multiple (typically two) laser pulses with focal spot displacement, multiple magnetic bubbles can be generated with which the Biermann magnetic field can be reconnected. Most relevant laser experiments have been devoted to this style of magnetic reconnection, in which the ablated plasmas strongly drive the magnetic reconnections.

In Section 4, we followed up on laser experiments applying external magnetic fields. Plasma propagations under the influence of external magnetic fields are dependent on the plasma β, the angle between the plasma propagation direction and the magnetic field orientation, and the experimental configuration. High-β plasma can evacuate the magnetic field regardless of the magnetic field orientation, following flute-type instabilities after the plasma kinetic pressure and the evacuated magnetic pressure balance in the perpendicular magnetic field configuration. Low-β parallel-propagating plasma can be well confined by the parallel magnetic field, forming a plasma jet. Low-β perpendicular-propagating plasma also shows plasma collimation on the kinetic scale.

In Section 5, we introduced our recent efforts on magnetic reconnection driven by electron dynamics in laser-produced plasmas. By applying a weak external magnetic field to a laser-produced plasma, we created magnetized electrons and unmagnetized ions, i.e., only the electrons were directly coupled with the magnetic field. Under this condition, plasma collimation was observed with global imaging, indicating that the magnetic field was distorted by the plasma dynamics pressure, resulting in a local anti-parallel magnetic field configuration. A plasmoid associated with cusp-like features was imaged through the plasma emissions, with the plasmoid propagating at the Alfvén velocity defined by the electron mass. This strongly indicates that the magnetic reconnection was driven by electron dynamics.

In Section 6, we further developed our electron-scale reconnection experiment to measure the local properties of plasmas and magnetic fields. In astrophysical plasmas, macroscopic information can be obtained by global imaging from distant astrophysical phenomena, but it is impossible to obtain local information. On the contrary, in space plasmas, microscopic information can be obtained by in-situ observations, such as of the Earth ' s magnetosphere with spacecraft, but it is difficult to obtain global information with point observations. It is therefore difficult to obtain microscopic and macroscopic information at the same time both in space and astrophysical plasmas, but laboratory experiments allow us to obtain both of these simultaneously. Electron outflows not accompanied by ion motion have been identified in the magnetic reconnection driven by electron dynamics. Magnetic field reversals and whistler waves also indicate magnetic reconnection on the electron scale.

We have been working on Thomson scattering measurements of nonlinear, non-stationary, and non-equilibrium plasmas to understand the instabilities and particle acceleration in such plasmas relevant to electron-scale magnetic reconnections.

Conflict of interest.   On behalf of all authors, the corresponding author states that there is no conflict of interest.

References

Bale, S.D., F.S. Mozer, and T. Phan. 2002, December. Observation of lower hybrid drift instability in the diffusion region at a reconnecting magnetopause. *Geophysical Research Letters 29*(24): 33–1–33–4. https://doi.org/10.1029/2002GL016113 .

Birdsall, C. and A. Langdon. 1991. *Plasma Physics via Computer Simulation* (1st ed.). CRC Press.

Birn, J. 2005. Forced magnetic reconnection. *Geophysical Research Letters 32*(6): L06105. https://doi.org/10.1029/2004GL022058 .

Birn, J., J.F. Drake, M.A. Shay, B.N. Rogers, R.E. Denton, M. Hesse, M. Kuznetsova, Z.W. Ma, A. Bhattacharjee, A. Otto, and P.L. Pritchett. 2001, March. Geospace Environmental Modeling (GEM) Magnetic Reconnection Challenge. *Journal of Geophysical Research: Space Physics 106*(A3): 3715–3719. https://doi.org/10.1029/1999JA900449 .

Biskamp, D. 1986. Magnetic reconnection via current sheets. *Physics of Fluids 29*(5): 1520. https://doi.org/10.1063/1.865670 .

Biskamp, D. 2000, September. *Magnetic Reconnection in Plasmas* (First ed.). Cambridge University Press.

Biskamp, D., E. Schwarz, and J.F. Drake. 1997, April. Two-fluid theory of collisionless magnetic reconnection. *Physics of Plasmas 4*(4): 1002–1009. https://doi.org/10.1063/1.872211 .

Borg, A.L., M. Øieroset, T.D. Phan, F.S. Mozer, A. Pedersen, C. Mouikis, J.P. McFadden, C. Twitty, A. Balogh, and H. Rème. 2005, October. Cluster encounter of a magnetic reconnection diffusion region in the near-Earth magnetotail on September 19, 2003. *Geophysical Research Letters 32*(19). https://doi.org/10.1029/2005GL023794 .

Burch, J.L., T.E. Moore, R.B. Torbert, and B.L. Giles. 2016. Magnetospheric multiscale overview and science objectives. *Space Science Reviews 199*(1): 5–21. https://doi.org/10.1007/s11214-015-0164-9 .

Burch, J.L., R.B. Torbert, T.D. Phan, L.J. Chen, T.E. Moore, R.E. Ergun, J.P. Eastwood, D.J. Gershman, P.A. Cassak, M.R. Argall, S. Wang, M. Hesse, C.J. Pollock, B.L. Giles, R. Nakamura, B.H. Mauk, S.A. Fuselier, C.T. Russell, R.J. Strangeway, J.F. Drake, M.A. Shay, Y.V. Khotyaintsev, P.A. Lindqvist, G. Marklund, F.D. Wilder, D.T. Young, K. Torkar, J. Goldstein, J.C. Dorelli, L.A. Avanov, M. Oka, D.N. Baker, A.N. Jaynes, K.A. Goodrich, I.J. Cohen, D.L. Turner, J.F. Fennell, J.B. Blake, J. Clemmons, M. Goldman, D. Newman, S.M. Petrinec, K.J. Trattner, B. Lavraud, P.H. Reiff, W. Baumjohann, W. Magnes, M. Steller, W. Lewis, Y. Saito, V. Coffey, and M. Chandler. 2016a. Electron-scale measurements of magnetic reconnection in space. *Science 352*(6290). https://doi.org/10.1126/science.aaf2939. http://science.sciencemag.org/content/352/6290/aaf2939.full.pdf .

Burch, J.L., R.B. Torbert, T.D. Phan, L.J. Chen, T.E. Moore, R.E. Ergun, J.P. Eastwood, D.J. Gershman, P.A. Cassak, M.R. Argall, S. Wang, M. Hesse, C.J. Pollock, B.L. Giles, R. Nakamura, B.H. Mauk, S.A. Fuselier, C.T. Russell, R.J. Strangeway, J.F. Drake, M.A. Shay, Y.V. Khotyaintsev, P.A. Lindqvist, G. Marklund, F.D. Wilder, D.T. Young, K. Torkar, J. Goldstein, J.C. Dorelli, L.A. Avanov, M. Oka, D.N. Baker, A.N. Jaynes, K.A. Goodrich, I.J. Cohen, D.L. Turner, J.F. Fennell, J.B. Blake, J. Clemmons, M. Goldman, D. Newman, S.M. Petrinec, K.J. Trattner, B. Lavraud, P.H. Reiff, W. Baumjohann, W. Magnes, M. Steller, W. Lewis, Y. Saito, V. Coffey, and M. Chandler. 2016b. Electron-scale measurements of magnetic reconnection in space. *Science 352*(6290): aaf2939. https://doi.org/10.1126/science.aaf2939. https://www.science.org/doi/pdf/10.1126/science.aaf2939 .

Carter, T.A., H. Ji, F. Trintchouk, M. Yamada, and R.M. Kulsrud. 2001, December. Measurement of Lower-Hybrid Drift Turbulence in a Reconnecting Current Sheet. *Physical Review Letters 88*(1): 015001. https://doi.org/10.1103/PhysRevLett.88.015001 .

Cassak, P.A., J.F. Drake, and M.A. Shay. 2006, June. A Model for Spontaneous Onset of Fast Magnetic Reconnection. *The Astrophysical Journal 644*(2): L145–L148. https://doi.org/10.1086/505690 .

Cassak, P.A., Y.H. Liu, and M.A. Shay. 2017, October. A review of the 0.1 reconnection rate problem. *Journal of Plasma Physics 83*(5). https://doi.org/10.1017/S0022377817000666 .

Chapman, I.T., R. Scannell, W.A. Cooper, J.P. Graves, R.J. Hastie, G. Naylor, and A. Zocco. 2010, December. Magnetic Reconnection Triggering Magnetohydrodynamic Instabilities during a Sawtooth Crash in a Tokamak Plasma. *Physical Review Letters 105*(25): 255002. https://doi.org/10.1103/PhysRevLett.105.255002 .

Chaston, C.C., J.R. Johnson, M. Wilber, M. Acuna, M.L. Goldstein, and H. Reme. 2009, January. Kinetic Alfvén Wave Turbulence and Transport through a Reconnection Diffusion Region. *Physical Review Letters 102*(1): 015001. https://doi.org/10.1103/PhysRevLett.102.015001 .

Chen, P.F. 2011. Coronal Mass Ejections: Models and Their Observational Basis. *Living Reviews in Solar Physics* 8. https://doi.org/10.12942/lrsp-2011-1 .

Cheng, C.Z., Y. Ren, G.S. Choe, and Y.J. Moon. 2003, October. Flux Rope Acceleration and Enhanced Magnetic Reconnection Rate. *The Astrophysical Journal 596*(2): 1341–1346. https://doi.org/10.1086/378170 .

Chien, A., L. Gao, S. Zhang, H. Ji, E.G. Blackman, W. Daughton, A. Stanier, A. Le, F. Guo, R. Follett, H. Chen, G. Fiksel, G. Bleotu, R.C. Cauble, S.N. Chen, A. Fazzini, K. Flippo, O. French, D.H. Froula, J. Fuchs, S. Fujioka, K. Hill, S. Klein, C. Kuranz, P. Nilson, A. Rasmus, and R. Takizawa. 2023. Non-thermal electron acceleration from magnetically driven reconnection in a laboratory plasma. *Nature Physics*. https://doi.org/10.1038/s41567-022-01839-x .

Contel, L., F. Sahraoui, A. Roux, D. Fontaine, P. Robert, J.A. Sauvaud, C. Owen, and A. Fazakerley. 2006. Small scale cluster observations of current sheet disruptions during substorm. *Int. Conf. Substorms-8*: 143 .

Courtois, C., R.A.D. Grundy, A.D. Ash, D.M. Chambers, N.C. Woolsey, R.O. Dendy, and K.G. McClements. 2004, July. Experiment on collisionless plasma interaction with applications to supernova remnant physics. *Physics of Plasmas* 11: 3386–3393. https://doi.org/10.1063/1.1752930 .

Dahlburg, R.B., S.K. Antiochos, and T.A. Zang. 1992, December. Secondary instability in three-dimensional magnetic reconnection. *Physics of Fluids B: Plasma Physics 4*(12): 3902–3914. https://doi.org/10.1063/1.860347 .

Daughton, W. 1999, April. The unstable eigenmodes of a neutral sheet. *Physics of Plasmas 6*(4): 1329–1343. https://doi.org/10.1063/1.873374 .

Daughton, W. 2002, September. Nonlinear dynamics of thin current sheets. *Physics of Plasmas 9*(9): 3668–3678. https://doi.org/10.1063/1.1499118 .

Daughton, W. and H. Karimabadi. 2005. Kinetic theory of collisionless tearing at the magnetopause. *Journal of Geophysical Research 110*(A3): A03217. https://doi.org/10.1029/2004JA010751 .

Daughton, W., V. Roytershteyn, H. Karimabadi, L. Yin, B.J. Albright, B. Bergen, and K.J. Bowers. 2011, July. Role of electron physics in the development of turbulent magnetic reconnection in collisionless plasmas. *Nature Physics 7*(7): 539–542. https://doi.org/10.1038/nphys1965 .

Daughton, W., J. Scudder, and H. Karimabadi. 2006, July. Fully kinetic simulations of undriven magnetic reconnection with open boundary conditions. *Physics of Plasmas 13*(7): 072101. https://doi.org/10.1063/1.2218817 .

Davidson, R.C. and N.T. Gladd. 1975. Anomalous transport properties associated with the lower-hybrid-drift instability. *Physics of Fluids 18*(10): 1327. https://doi.org/10.1063/1.861021 .

Davidson, R.C., N.T. Gladd, C.S. Wu, and J.D. Huba. 1977. Effects of finite plasma beta on the lower-hybrid-drift instability. *Physics of Fluids 20*(2): 301. https://doi.org/10.1063/1.861867 .

Dimonte, G. and L.G. Wiley. 1991, September. Dynamics of exploding plasmas in a magnetic field. *Physical Review Letters* 67: 1755–1758. https://doi.org/10.1103/PhysRevLett.67.1755 .

Dong, Q.L., S.J. Wang, Q.M. Lu, C. Huang, D.W. Yuan, X. Liu, X.X. Lin, Y.T. Li, H.G. Wei, J.Y. Zhong, J.R. Shi, S.E. Jiang, Y.K. Ding, B.B. Jiang, K. Du, X.T. He, M.Y. Yu, C.S. Liu, S. Wang, Y.J. Tang, J.Q. Zhu, G. Zhao, Z.M. Sheng, and J. Zhang. 2012, May. Plasmoid ejection and secondary current sheet generation from magnetic reconnection in laser-plasma interaction. *Phys. Rev. Lett.* 108: 215001. https://doi.org/10.1103/PhysRevLett.108.215001 .

Drake, J.F. 1981. Magnetic field diffusion and dissipation in reversed-field plasmas. *Physics of Fluids 24*(1): 78. https://doi.org/10.1063/1.863249 .

Drake, J.F., P.A. Cassak, M.A. Shay, M. Swisdak, and E. Quataert. 2009, July. A magnetic reconnection mechanism for ion acceleration and abundance enhancements in impulsive flares. *The Astrophysical Journal 700*(1): L16–L20. https://doi.org/10.1088/0004-637X/700/1/L16 .

Drake, J.F., M.A. Shay, and M. Swisdak. 2008. The Hall fields and fast magnetic reconnection. *Physics of Plasmas 15*(4): 042306. https://doi.org/10.1063/1.2901194 .

Drake, J.F., M.A. Shay, W. Thongthai, and M. Swisdak. 2005, Mar. Production of energetic electrons during magnetic reconnection. *Phys. Rev. Lett.* 94: 095001. https://doi.org/10.1103/PhysRevLett.94.095001 .

Egedal, J., A. Le, and W. Daughton. 2013, June. A review of pressure anisotropy caused by electron trapping in collisionless plasma, and its implications for magnetic reconnection. *Physics of Plasmas 20*(6): 061201. https://doi.org/10.1063/1.4811092 .

Everson, E.T., P. Pribyl, C.G. Constantin, A. Zylstra, D. Schaeffer, N.L. Kugland, and C. Niemann. 2009, November. Design, construction, and calibration of a three-axis, high-frequency magnetic probe (B-dot probe) as a diagnostic for exploding plasmas. *Review of Scientific Instruments 80*(11): 113505–+. https://doi.org/10.1063/1.3246785 .

Faenov, A., V. Dyakin, A. Magunov, T. Pikuz, I. Skobelev, S. Pikuz, A. Kasperczyk, T. Pisarczyk, J. Wolowski, and E. Zielinska. 1996, May. Using x-ray spectroheliograph technique for investigations of laser-produced plasma under interaction with strong magnetic field. Phys. Scr 53: 591–596. https://doi.org/10.1088/0031-8949/53/5/016 .

Froula, S.H., S.H. Glenzer, N.C.J. Luhmann, and J. Sheffield. 2011. *Plasma Scattering of Electromagnetic Radiation: Theory and Measurement Techniques.* Amsterdam: Elsevier.

Fu, X.R., Q.M. Lu, and S. Wang. 2006, 01. The process of electron acceleration during collisionless magnetic reconnection. *Physics of Plasmas 13*(1): 012309. https://doi.org/10.1063/1.2164808. https://pubs.aip.org/aip/pop/article-pdf/doi/10.1063/1.2164808/15983511/012309_1_online.pdf .

Fujimoto, K. 2014. Wave activities in separatrix regions of magnetic reconnection. *Geophysical Research Letters 41*(8): 2721–2728. https://doi.org/doi.org/10.1002/2014GL059893 .

Fujimoto, K. and R.D. Sydora. 2008. Whistler waves associated with magnetic reconnection. *Geophysical Research Letters 35*(19). https://doi.org/10.1029/2008GL035201 .

Fujimoto, K. and R.D. Sydora. 2017, May. Linear theory of the current sheet shear instability. *Journal of Geophysical Research: Space Physics 122*(5): 5418–5430. https://doi.org/10.1002/2017JA024079 .

Fujimoto, K. and R.D. Sydora. 2021, March. Electromagnetic Turbulence in the Electron Current Layer to Drive Magnetic Reconnection. *The Astrophysical Journal Letters 909*(1): L15. https://doi.org/10.3847/2041-8213/abe877 .

Gary, S.P. 1980. Wave-particle transport from electrostatic instabilities. *Physics of Fluids 23*(6): 1193. https://doi.org/10.1063/1.863120 .

Gurnett, D.A., L.A. Frank, and R.P. Lepping. 1976, December. Plasma waves in the distant magnetotail. *Journal of Geophysical Research 81*(34): 6059–6071. https://doi.org/10.1029/JA081i034p06059 .

Harilal, S.S., M.S. Tillack, B. O'Shay, C.V. Bindhu, and F. Najmabadi. 2004, February. Confinement and dynamics of laser-produced plasma expanding across a transverse magnetic field. Phys. Rev. E *69*(2): 026413–+. https://doi.org/10.1103/PhysRevE.69.026413 .

Harris, E.G. 1962, January. On a plasma sheath separating regions of oppositely directed magnetic field. *Il Nuovo Cimento 23*(1): 115–121. https://doi.org/10.1007/BF02733547 .

Hesse, M., J. Birn, and M. Kuznetsova. 2001, March. Collisionless magnetic reconnection: Electron processes and transport modeling. *Journal of Geophysical Research: Space Physics 106*(A3): 3721–3735. https://doi.org/10.1029/1999JA001002 .

Hesse, M., K. Schindler, J. Birn, and M. Kuznetsova. 1999, May. The diffusion region in collisionless magnetic reconnection. *Physics of Plasmas 6*(5): 1781–1795. https://doi.org/10.1063/1.873436 .

Horiuchi, R. and H. Ohtani. 2008. Formation of non-maxwellian distribution and its role in collisionless driven reconnection. *Communications in Computational Physics* 4: 496–505 .

Horiuchi, R. and T. Sato. 1990, November. The meandering orbit effect on stabilization of the tilting instability in a field-reversed configuration. *Physics of Fluids B: Plasma Physics 2*(11): 2652–2660. https://doi.org/10.1063/1.859579 .

Horiuchi, R. and T. Sato. 1997, February. Particle simulation study of collisionless driven reconnection in a sheared magnetic field. *Physics of Plasmas* 4: 277–289. https://doi.org/10.1063/1.872088 .

Horiuchi, R. and T. Sato. 1997, February. Particle simulation study of collisionless driven reconnection in a sheared magnetic field. *Physics of Plasmas 4*(2): 277–289. https://doi.org/10.1063/1.872088 .

Horiuchi, R. and T. Sato. 1999, December. Three-dimensional particle simulation of plasma instabilities and collisionless reconnection in a current sheet. *Physics of Plasmas 6*(12): 4565–4574. https://doi.org/10.1063/1.873744 .

Hornig, G. and K. Schindler. 1996, March. Magnetic topology and the problem of its invariant definition. *Physics of Plasmas 3*(3): 781–791. https://doi.org/10.1063/1.871778 .

Hsia, J.B., S.M. Chiu, M.F. Hsia, R.L. Chou, and C.S. Wu. 1979. Generalized lower-hybrid-drift instability. *Physics of Fluids 22*(9): 1737. https://doi.org/10.1063/1.862810 .

Huba, J.D., J.F. Drake, and N.T. Gladd. 1980. Lower-hybrid-drift instability in field reversed plasmas. *Physics of Fluids 23*(3): 552. https://doi.org/10.1063/1.863003 .

Huba, J.D., N.T. Gladd, and K. Papadopoulos. 1977, March. The lower-hybrid-drift instability as a source of anomalous resistivity for magnetic field line reconnection. *Geophysical Research Letters 4*(3): 125–128. https://doi.org/10.1029/GL004i003p00125 .

Huba, J.D., N.T. Gladd, and K. Papadopoulos. 1978. Lower-hybrid-drift wave turbulence in the distant magnetotail. *Journal of Geophysical Research 83*(A11): 5217. https://doi.org/10.1029/JA083iA11p05217 .

Huba, J.D. and L.I. Rudakov. 2004, October. Hall Magnetic Reconnection Rate. *Physical Review Letters 93*(17): 175003. https://doi.org/10.1103/PhysRevLett.93.175003 .

Ishizawa, A. and R. Horiuchi. 2005, July. Suppression of Hall-Term Effects by Gyroviscous Cancellation in Steady Collisionless Magnetic Reconnection. *Physical Review Letters 95*(4): 045003. https://doi.org/10.1103/PhysRevLett.95.045003 .

Ishizawa, A., R. Horiuchi, and H. Ohtani. 2004, July. Two-scale structure of the current layer controlled by meandering motion during steady-state collisionless driven reconnection. *Physics of Plasmas* 11: 3579–3585. https://doi.org/10.1063/1.1758718 .

Ishizawa, A., R. Horiuchi, and H. Ohtani. 2004, July. Two-scale structure of the current layer controlled by meandering motion during steady-state collisionless driven reconnection. *Physics of Plasmas 11*(7): 3579–3585. https://doi.org/10.1063/1.1758718 .

Isobe, H. and K. Shibata. 2009, June. Reconnection in solar flares: Outstanding questions. *Journal of Astrophysics and Astronomy 30*(2): 79–85. https://doi.org/10.1007/s12036-009-0007-8 .

Janvier, M. 2017, February. Three-dimensional magnetic reconnection and its application to solar flares. *Journal of Plasma Physics 83*(1): 535830101. https://doi.org/10.1017/S0022377817000034 .

Ji, H., J. Karpen, A. Alt, S. Antiochos, S. Baalrud, S. Bale, P.M. Bellan, M. Begelman, A. Beresnyak, A. Bhattacharjee, E.G. Blackman, D. Brennan, M. Brown, J. Buechner, J. Burch, P. Cassak, B. Chen, L.J. Chen, Y. Chen, A. Chien, L. Comisso, D. Craig, J. Dahlin, W. Daughton, E. DeLuca, C.F. Dong, S. Dorfman, J. Drake, F. Ebrahimi, J. Egedal, R. Ergun, G. Eyink, Y. Fan, G. Fiksel, C. Forest, W. Fox, D. Froula, K. Fujimoto, L. Gao, K. Genestreti, S. Gibson, M. Goldstein, F. Guo, J. Hare, M. Hesse, M. Hoshino, Q. Hu, Y.M. Huang, J. Jara-Almonte, H. Karimabadi, J. Klimchuk, M. Kunz, K. Kusano, A. Lazarian, A. Le, S. Lebedev, H. Li, X. Li, Y. Lin, M. Linton, Y.H. Liu, W. Liu, D. Longcope, N. Loureiro, Q.M. Lu, Z.W. Ma, W.H. Matthaeus, D. Meyerhofer, F. Mozer, T. Munsat, N.A. Murphy, P. Nilson, Y. Ono, M. Opher, H. Park, S. Parker, M. Petropoulou, T. Phan, S. Prager, M. Rempel, C. Ren, Y. Ren, R. Rosner, V. Roytershteyn, J. Sarff, A. Savcheva, D. Schaffner, K. Schoeffier, E. Scime, M. Shay, L. Sironi, M. Sitnov, A. Stanier, M. Swisdak, J. TenBarge, T. Tharp, D. Uzdensky, A. Vaivads, M. Velli, E. Vishniac, H. Wang, G. Werner, C. Xiao, M. Yamada, T. Yokoyama, J. Yoo, S. Zenitani, and E. Zweibel. 2020, September. Major Scientific Challenges and Opportunities in Understanding Magnetic Reconnection and Related Explosive Phenomena in Solar and Heliospheric Plasmas.

Ji, H., S. Terry, M. Yamada, R. Kulsrud, A. Kuritsyn, and Y. Ren. 2004, Mar. Electromagnetic fluctuations during fast reconnection in a laboratory plasma. *Phys. Rev. Lett.* 92: 115001. https://doi.org/10.1103/PhysRevLett. 92.115001 .

Karimabadi, H. 2004. On magnetic reconnection regimes and associated three-dimensional asymmetries: Hybrid, Hall-less hybrid, and Hall-MHD simulations. *Journal of Geophysical Research 109*(A9): A09205. https://doi.org/10.1029/2004JA010478 .

Khasanah, N., C. Peng, C. Chen, T. Huang, N. Bolouki, T. Moritaka, Y. Hara, H. Shimogawara, T. Sano, Y. Sakawa, Y. Sato, K. Tomita, K. Uchino, S. Matsukiyo, Y. Shoji, S. Tomita, S. Tomiya, R. Yamazaki, M. Koenig, and Y. Kuramitsu. 2017. Spatial and temporal plasma evolutions of magnetic reconnection in laser produced plasmas. *High Energy Density Physics* 23: 15 – 19. https://doi.org/http://dx.doi.org/10.1016/j.hedp.2017.02.004 .

Kulsrud, R., H. Ji, W. Fox, and M. Yamada. 2005, August. An electromagnetic drift instability in the magnetic reconnection experiment and its importance for magnetic reconnection. *Physics of Plasmas 12*(8): 082301. https://doi. org/10.1063/1.1949225 .

Kuramitsu, Y., H.H. Chu, L.N. Hau, S.H. Chen, Y.L. Liu, C.Y. Hsieh, Y. Sakawa, T. Hideaki, and J. Wang. 2015. Relativistic plasma astrophysics with intense lasers. *High Energy Density Physics* 17, Part A: 198 – 202. https://doi.org/http://dx.doi.org/10.1016/j.hedp.2014.11.005 .

Kuramitsu, Y., S. Matsukiyo, S. Isayama, D. Harada, T. Oyama, R. Fujino, Y. Sakawa, T. Morita, Y. Yamaura, T. Ishikawa, T. Moritaka, T. Sano, K. Tomita, R. Shimoda, Y. Sato, K. Uchino, A. Pelka, R. Crowston, N. Woolsey, G. Gregori, M. Koenig, D.W. Yuan, C.L. Yin, Y.T. Li, K. Zhang, J.Y. Zhong, F.L. Wang, N. Ohnishi, K. Nagamine, H. Yoneda, and H. Takabe. 2016. Spherical shock in the presence of an external magnetic field. *Journal of Physics: Conference Series 688*(1): 012056 .

Kuramitsu, Y., T. Moritaka, Y. Sakawa, T. Morita, T. Sano, M. Koenig, C.D. Gregory, N. Woolsey, K. Tomita, H. Takabe, Y.L. Liu, S.H. Chen, S. Matsukiyo, and M. Hoshino. 2018. Magnetic reconnection driven by electron dynamics. *Nature Communications 9*(1): 5109. https://doi.org/10.1038/s41467-018-07415-3 .

Kuramitsu, Y., N. Ohnishi, Y. Sakawa, T. Morita, H. Tanji, T. Ide, K. Nishio, C.D. Gregory, J.N. Waugh, N. Booth, R. Heathcote, C. Murphy, G. Gregori, J. Smallcombe, C. Barton, A. Dizière, M. Koenig, N. Woolsey, Y. Matsumoto, A. Mizuta, T. Sugiyama, S. Matsukiyo, T. Moritaka, T. Sano, and H. Takabe. 2016. Model experiment of magnetic field amplification in laser-produced plasmas via the richtmyer-meshkov instability. *Physics of Plasmas 23*(3). https://doi.org/http://dx.doi.org/10.1063/1.4944925 .

Kuramitsu, Y., Y. Sakawa, T. Morita, S. Dono, H. Aoki, H. Tanji, C.D. Gregory, J.N. Waugh, B. Loupias, M. Koenig, N. Woolsey, T. Ide, T. Sano, and H. Takabe. 2011, November. Formation of density inhomogeneity in laser produced plasmas for a test bed of magnetic field amplification in supernova remnants. Ap&SS 336: 269–272. https://doi.org/10.1007/s10509-010-0568-7 .

Kuramitsu, Y., Y. Sakawa, T. Morita, T. Ide, K. Nishio, H. Tanji, H. Aoki, S. Dono, C.D. Gregory, J.N. Waugh, N. Woolsey, A. Diziere, A. Pelka, A. Ravasio, B. Loupias, M. Koenig, S.A. Pikuz, Y.T. Li, Y. Zhang, X. Liu, J.Y. Zhong, J. Zhang, G. Gregori, N. Nakanii, K. Kondo, Y. Mori, E. Miura, R. Kodama, Y. Kitagawa, K. Mima, K.A. Tanaka, H. Azechi, T. Moritaka, Y. Matsumoto, T. Sano, A. Mizuta, N. Ohnishi, M. Hoshino, and H. Takabe. 2012. Laboratory investigations on the origins of cosmic rays. *Plasma Physics and Controlled Fusion 54*(12): 124049 .

Kuramitsu, Y., Y. Sakawa, J.N. Waugh, C.D. Gregory, T. Morita, S. Dono, H. Aoki, H. Tanji, B. Loupias, M. Koenig, N. Woolsey, and H. Takabe. 2009, December. Jet Formation in Counterstreaming Collisionless Plasmas.

ApJ 707: L137–L141. https://doi.org/10.1088/0004-637X/707/2/L137 .

Lapenta, G. and J.U. Brackbill. 1997, December. A kinetic theory for the drift-kink instability. *Journal of Geophysical Research: Space Physics 102*(A12): 27099–27108. https://doi.org/10.1029/97JA02140 .

Lapenta, G. and J.U. Brackbill. 2002, May. Nonlinear evolution of the lower hybrid drift instability: Current sheet thinning and kinking. *Physics of Plasmas 9*(5): 1544–1554. https://doi.org/10.1063/1.1464149 .

Lapenta, G., J.U. Brackbill, and W.S. Daughton. 2003, May. The unexpected role of the lower hybrid drift instability in magnetic reconnection in three dimensions. *Physics of Plasmas 10*(5): 1577–1587. https://doi.org/10.1063/1.1560615 .

Le, A., A. Stanier, W. Daughton, J. Ng, J. Egedal, W.D. Nystrom, and R. Bird. 2019, October. Three-dimensional stability of current sheets supported by electron pressure anisotropy. *Physics of Plasmas 26*(10): 102114. https://doi.org/10.1063/1.5125014 .

Li, X., R. Wang, Q. Lu, K.J. Hwang, Q. Zong, C.T. Russell, and S. Wang. 2019. Observation of nongyrotropic electron distribution across the electron diffusion region in the magnetotail reconnection. *Geophysical Research Letters 46*(24): 14263–14273. https://doi.org/https://doi.org/10.1029/2019GL085014. https://agupubs.onlinelibrary.wiley.com/doi/pdf/10.1029/2019GL085014 .

Liu, D., K. Huang, Q. Lu, S. Lu, R. Wang, W. Ding, and S. Wang. 2021, nov. The evolution of collisionless magnetic reconnection from electron scales to ion scales. *The Astrophysical Journal 922*(1): 51. https://doi.org/10.3847/1538-4357/ac2900 .

Liu, D., S. Lu, Q. Lu, W. Ding, and S. Wang. 2020, feb. Spontaneous onset of collisionless magnetic reconnection on an electron scale. *The Astrophysical Journal Letters 890*(2): L15. https://doi.org/10.3847/2041-8213/ab72fe .

Loureiro, N.F. and D.A. Uzdensky. 2016, January. Magnetic reconnection: From the Sweet–Parker model to stochastic plasmoid chains. *Plasma Physics and Controlled Fusion 58*(1): 014021. https://doi.org/10.1088/0741-3335/58/1/014021 .

Lu, Q., Z. Yang, H. Wang, R. Wang, K. Huang, S. Lu, and S. Wang. 2021, sep. Two-dimensional particle-in-cell simulation of magnetic reconnection in the downstream of a quasi-perpendicular shock. *The Astrophysical Journal 919*(1): 28. https://doi.org/10.3847/1538-4357/ac18c0 .

Lu, S., Q. Lu, R. Wang, P.L. Pritchett, M. Hubbert, Y. Qi, K. Huang, X. Li, and C.T. Russell. 2022. Electron-only reconnection as a transition from quiet current sheet to standard reconnection in earth's magnetotail: Particle-in-cell simulation and application to mms data. *Geophysical Research Letters 49*(11): e2022GL098547. https://doi.org/https://doi.org/10.1029/2022GL098547. https://agupubs.onlinelibrary.wiley.com/doi/pdf/10.1029/2022GL098547 .

Lu, S., R. Wang, Q. Lu, V. Angelopoulos, R. Nakamura, A.V. Artemyev, P.L. Pritchett, T.Z. Liu, X.J. Zhang, W. Baumjohann, W. Gonzalez, A.C. Rager, R.B. Torbert, B.L. Giles, D.J. Gershman, C.T. Russell, R.J. Strangeway, Y. Qi, R.E. Ergun, P.A. Lindqvist, J.L. Burch, and S. Wang. 2020. Magnetotail reconnection onset caused by electron kinetics with a strong external driver. *Nature Communications 11*(1): 5049. https://doi.org/10.1038/s41467-020-18787-w .

Lui, A. 2000. Tutorial on geomagnetic storms and substorms. *IEEE Transactions on Plasma Science 28*(6): 1854–1866. https://doi.org/10.1109/27.902214 .

Ma, Z.W. and A. Bhattacharjee. 2001, March. Hall magnetohydrodynamic reconnection: The Geospace Environment Modeling challenge. *Journal of Geophysical Research: Space Physics 106*(A3): 3773–3782. https://doi.org/10.1029/1999JA001004 .

Mabey, P., B. Albertazzi, E. Falize, T. Michel, G. Rigon, L. Van Box Som, A. Pelka, F.E. Brack, F. Kroll, E. Filippov, G. Gregori, Y. Kuramitsu, D.Q. Lamb, C. Li, N. Ozaki, S. Pikuz, Y. Sakawa, P. Tzeferacos, and M. Koenig. 2019. Laboratory study of stationary accretion shock relevant to astrophysical systems. *Scientific Reports 9*(1): 8157. https://doi.org/10.1038/s41598-019-44596-3 .

Malkov, M.A. and V.I. Sotnikov. 1981. Current-driven instability of large-β drift waves in the magnetosphere. *Soviet Journal of Plasma Physics* 7: 405 .

Matsukiyo, S., Y. Kuramitsu, and K. Tomita. 2016. Collective scattering of an incident monochromatic circularly polarized wave in an unmagnetized non-equilibrium plasma. *Journal of Physics: Conference Series 688*(1): 012062 .

Matsukiyo, S., R. Yamazaki, T. Morita, K. Tomita, Y. Kuramitsu, T. Sano, S.J. Tanaka, T. Takezaki, S. Isayama, T. Higuchi, H. Murakami, Y. Horie, N. Katsuki, R. Hatsuyama, M. Edamoto, H. Nishioka, M. Takagi, T. Kojima, S. Tomita, N. Ishizaka, S. Kakuchi, S. Sei, K. Sugiyama, K. Aihara, S. Kambayashi, M. Ota, S. Egashira, T. Izumi, T. Minami, Y. Nakagawa, K. Sakai, M. Iwamoto, N. Ozaki, and Y. Sakawa. 2022, Aug. High-power laser experiment on developing supercritical shock propagating in homogeneously

magnetized plasma of ambient gas origin. *Phys. Rev. E* 106: 025205. https://doi.org/10.1103/PhysRevE.106.025205 .

Matthaeus, W.H. and S.L. Lamkin. 1986, 08. Turbulent magnetic reconnection. *The Physics of Fluids 29*(8): 2513–2534. https://doi.org/10.1063/1.866004. https://pubs.aip.org/aip/pfl/article-pdf/29/8/2513/12477152/2513_1_online.pdf .

Moritaka, T. and R. Horiuchi. 2008, September. Roles of ion and electron dynamics in the onset of magnetic reconnection due to current sheet instabilities. *Physics of Plasmas 15*(9): 092114. https://doi.org/10.1063/1.2979316 .

Moritaka, T., R. Horiuchi, and H. Ohtani. 2007, October. Anomalous resistivity due to kink modes in a thin current sheet. *Physics of Plasmas 14*(10): 102109. https://doi.org/10.1063/1.2767623 .

Moritaka, T., Y. Kuramitsu, Y.L. Liu, and S.H. Chen. 2016, March. Spontaneous focusing of plasma flow in a weak perpendicular magnetic field. *Physics of Plasmas 23*(3): 032110. https://doi.org/10.1063/1.4942028 .

Mostovych, A.N., B.H. Ripin, and J.A. Stamper. 1989, June. Laser-produced plasma jets - Collimation and instability in strong transverse magnetic fields. *Physical Review Letters* 62: 2837–2840. https://doi.org/10.1103/PhysRevLett.62.2837 .

Mozer, F.S. 2005. Criteria for and statistics of electron diffusion regions associated with subsolar magnetic field reconnection. *Journal of Geophysical Research 110*(A12): A12222. https://doi.org/10.1029/2005JA011258 .

Mozer, F.S., O.A. Agapitov, A. Artemyev, J.L. Burch, R.E. Ergun, B.L. Giles, D. Mourenas, R.B. Torbert, T.D. Phan, and I. Vasko. 2016, Apr. Magnetospheric multiscale satellite observations of parallel electron acceleration in magnetic field reconnection by fermi reflection from time domain structures. *Phys. Rev. Lett.* 116: 145101. https://doi.org/10.1103/PhysRevLett.116.145101 .

Mozer, F.S., S.D. Bale, and T.D. Phan. 2002, June. Evidence of Diffusion Regions at a Subsolar Magnetopause Crossing. *Physical Review Letters 89*(1): 015002. https://doi.org/10.1103/PhysRevLett.89.015002 .

Mozer, F.S., T.D. Phan, and S.D. Bale. 2003, June. The complex structure of the reconnecting magnetopause. *Physics of Plasmas 10*(6): 2480–2485. https://doi.org/10.1063/1.1570419 .

Muñoz, P.A. and J. Büchner. 2018, October. Kinetic turbulence in fast three-dimensional collisionless guide-field magnetic reconnection. *Physical Review*

E 98(4): 043205. https://doi.org/10.1103/PhysRevE.98.043205 .

Muñoz, P.A., D. Told, P. Kilian, J. Büchner, and F. Jenko. 2015, August. Gyrokinetic and kinetic particle-in-cell simulations of guide-field reconnection. I. Macroscopic effects of the electron flows. *Physics of Plasmas 22*(8): 082110. https://doi.org/10.1063/1.4928381 .

Nagai, T., I. Shinohara, M. Fujimoto, M. Hoshino, Y. Saito, S. Machida, and T. Mukai. 2001, November. Geotail observations of the Hall current system: Evidence of magnetic reconnection in the magnetotail. *Journal of Geophysical Research: Space Physics 106*(A11): 25929–25949. https://doi.org/10.1029/2001JA900038 .

Ng, J., J. Egedal, A. Le, W. Daughton, and L.J. Chen. 2011, February. Kinetic Structure of the Electron Diffusion Region in Antiparallel Magnetic Reconnection. *Physical Review Letters 106*(6): 065002. https://doi.org/10.1103/PhysRevLett.106.065002 .

Niemann, C., W. Gekelman, C.G. Constantin, E.T. Everson, D.B. Schaeffer, A.S. Bondarenko, S.E. Clark, D. Winske, S. Vincena, B. Van Compernolle, and P. Pribyl. 2014, November. Observation of collisionless shocks in a large current-free laboratory plasma. Geophys. Res. Lett. 41: 7413–7418. https://doi.org/10.1002/2014GL061820 .

Nilson, P.M., L. Willingale, M.C. Kaluza, C. Kamperidis, S. Minardi, M.S. Wei, P. Fernandes, M. Notley, S. Bandyopadhyay, M. Sherlock, R.J. Kingham, M. Tatarakis, Z. Najmudin, W. Rozmus, R.G. Evans, M.G. Haines, A.E. Dangor, and K. Krushelnick. 2006, December. Magnetic Reconnection and Plasma Dynamics in Two-Beam Laser-Solid Interactions. *Physical Review Letters 97*(25): 255001–+. https://doi.org/10.1103/PhysRevLett.97.255001 .

Nishio, K., Y. Sakawa, Y. Kuramitsu, T. Morita, T. Ide, M. Kuwada, M. Koga, T. Kato, T. Norimatsu, C. Gregory, N. Woolsey, C. Murphy, G. Gregori, K. Schaar, A. Diziere, M. Koenig, A. Pelka, S. Wang, Q. Dong, Y. Li, and H. Takabe. 2013. Laboratory experiments on plasma jets in a magnetic field using high-power lasers. *EPJ Web of Conferences* 59: 15005. https://doi.org/10.1051/epjconf/20135915005 .

Nishizuka, N., M. Shimizu, T. Nakamura, K. Otsuji, T.J. Okamoto, Y. Katsukawa, and K. Shibata. 2008, August. Giant Chromospheric Anemone Jet Observed with *Hinode* and Comparison with Magnetohydrodynamic Simulations: Evidence of Propagating Alfvén Waves and Magnetic Reconnection. *The Astrophysical Journal 683*(1): L83–L86. https://doi.org/10.1086/591445 .

Ono, Y., M. Inomoto, T. Okazaki, and Y. Ueda. 1997, May. Experimental investigation of three-component magnetic reconnection by use of merging spheromaks and tokamaks. *Physics of Plasmas 4*(5): 1953–1963. https:// doi.org/10.1063/1.872337 .

Onsager, T.G., M.F. Thomsen, J.T. Gosling, and S.J. Bame. 1990, October. Electron distributions in the plasma sheet boundary layer: Time-of-flight effects. *Geophysical Research Letters 17*(11): 1837–1840. https://doi.org/ 10.1029/GL017i011p01837 .

Otto, A. 2001, March. Geospace Environment Modeling (GEM) magnetic reconnection challenge: MHD and Hall MHD-constant and current dependent resistivity models. *Journal of Geophysical Research: Space Physics 106*(A3): 3751–3757. https://doi.org/10.1029/1999JA001005 .

Ozaki, M., T. Sato, R. Horiuchi, and the Complexity Simulation Group. 1996, June. Electromagnetic instability and anomalous resistivity in a magnetic neutral sheet. *Physics of Plasmas 3*(6): 2265–2274. https://doi.org/10. 1063/1.871908 .

Parker, E.N. 1957a, August. Newtonian Development of the Dynamical Properties of Ionized Gases of Low Density. *Physical Review 107*(4): 924–933. https://doi.org/10.1103/PhysRev.107.924 .

Parker, E.N. 1957b, December. Sweet's mechanism for merging magnetic fields in conducting fluids. *Journal of Geophysical Research 62*(4): 509–520. https://doi.org/10.1029/JZ062i004p00509 .

Pei, W., R. Horiuchi, and T. Sato. 2001, July. Long time scale evolution of collisionless driven reconnection in a two-dimensional open system. *Physics of Plasmas 8*(7): 3251–3257. https://doi.org/10.1063/1.1375150 .

Petschek, H.E. 1964, January. Magnetic Field Annihilation. *NASA Special Publication* 50: 425 .

Phan, T.D., J.P. Eastwood, M.A. Shay, J.F. Drake, B.U.Ö. Sonnerup, M. Fujimoto, P.A. Cassak, M. Øieroset, J.L. Burch, R.B. Torbert, A.C. Rager, J.C. Dorelli, D.J. Gershman, C. Pollock, P.S. Pyakurel, C.C. Haggerty, Y. Khotyaintsev, B. Lavraud, Y. Saito, M. Oka, R.E. Ergun, A. Retino, O. Le Contel, M.R. Argall, B.L. Giles, T.E. Moore, F.D. Wilder, R.J. Strangeway, C.T. Russell, P.A. Lindqvist, and W. Magnes. 2018, May. Electron magnetic reconnection without ion coupling in Earth's turbulent magnetosheath. Nature 557: 202–206. https://doi.org/10.1038/s41586-018-0091-5 .

Phan, T.D., J.P. Eastwood, M.A. Shay, J.F. Drake, B.U.Ö. Sonnerup, M. Fujimoto, P.A. Cassak, M. Øieroset, J.L. Burch, R.B. Torbert, A.C. Rager,

J.C. Dorelli, D.J. Gershman, C. Pollock, P.S. Pyakurel, C.C. Haggerty, Y. Khotyaintsev, B. Lavraud, Y. Saito, M. Oka, R.E. Ergun, A. Retino, O. Le Contel, M.R. Argall, B.L. Giles, T.E. Moore, F.D. Wilder, R.J. Strangeway, C.T. Russell, P.A. Lindqvist, and W. Magnes. 2018. Electron magnetic reconnection without ion coupling in earth's turbulent magnetosheath. *Nature 557*(7704): 202–206. https://doi.org/10.1038/s41586-018-0091-5 .

Phan, T.D., G. Paschmann, C. Twitty, F.S. Mozer, J.T. Gosling, J.P. Eastwood, M. Øieroset, H. Rème, and E.A. Lucek. 2007. Evidence for magnetic reconnection initiated in the magnetosheath. *Geophysical Research Letters 34*(14). https://doi.org/https://doi.org/10.1029/2007GL030343. https://agupubs.onlinelibrary.wiley.com/doi/pdf/10.1029/2007GL030343 .

Phan, T.D., M.A. Shay, C.C. Haggerty, J.T. Gosling, J.P. Eastwood, M. Fujimoto, K. Malakit, F.S. Mozer, P.A. Cassak, M. Oieroset, and V. Angelopoulos. 2016, September. Ion Larmor radius effects near a reconnection X line at the magnetopause: THEMIS observations and simulation comparison. *Geophysical Research Letters 43*(17): 8844–8852. https://doi.org/10.1002/2016GL070224 .

Ping, Y., J. Zhong, X. Wang, B. Han, W. Sun, Y. Zhang, D. Yuan, C. Xing, J. Wang, Z. Liu, Z. Zhang, B. Qiao, H. Zhang, Y. Li, J. Zhu, G. Zhao, and J. Zhang. 2023. Turbulent magnetic reconnection generated by intense lasers. *Nature Physics*. https://doi.org/10.1038/s41567-022-01855-x .

Pisarczyk, T., B.A. Bryunetkin, A.Y. Faenov, A. Farynski, H. Fiedorowicz, M.O. Koshevoy, R. Miklaszewski, M. Mroczkowski, M.V. Osipov, P. Parys, I.Y. Skobelev, and M. Szczurek. 1994, July. Influence of an external strong magnetic field on hydrodynamic parameters and radiation emission of laser produced plasma. Phys. Scr 50: 72–81. https://doi.org/10.1088/0031-8949/50/1/010 .

Plechaty, C., R. Presura, and A.A. Esaulov. 2013, Oct. Focusing of an explosive plasma expansion in a transverse magnetic field. *Phys. Rev. Lett.* 111: 185002. https://doi.org/10.1103/PhysRevLett.111.185002 .

Pontin, D.I. and E.R. Priest. 2022, December. Magnetic reconnection: MHD theory and modelling. *Living Reviews in Solar Physics 19*(1): 1. https://doi.org/10.1007/s41116-022-00032-9 .

Priest, E.R. and T.G. Forbes. 1986. New models for fast steady state magnetic reconnection. *Journal of Geophysical Research 91*(A5): 5579. https://doi.org/10.1029/JA091iA05p05579 .

Pritchett, P.L. 2001, March. Geospace Environment Modeling magnetic reconnection challenge: Simulations with a full particle electromagnetic

code. *Journal of Geophysical Research: Space Physics 106* (A3): 3783–3798. https://doi.org/10.1029/1999JA001006 .

Pucci, F., S. Usami, H. Ji, X. Guo, R. Horiuchi, S. Okamura, W. Fox, J. Jara-Almonte, M. Yamada, and J. Yoo. 2018, December. Energy transfer and electron energization in collisionless magnetic reconnection for different guide-field intensities. *Physics of Plasmas 25* (12): 122111. https://doi.org/10.1063/1.5050992 .

Pyakurel, P.S., M.A. Shay, J.F. Drake, T.D. Phan, P.A. Cassak, and J.L. Verniero. 2021, Oct. Faster form of electron magnetic reconnection with a finite length x-line. *Phys. Rev. Lett.* 127: 155101. https://doi.org/10.1103/PhysRevLett.127.155101 .

Ricci, P., G. Lapenta, and J.U. Brackbill. 2002. Gem reconnection challenge: Implicit kinetic simulations with the physical mass ratio. *Geophysical Research Letters 29* (23): 3–1–3–4. https://doi.org/https://doi.org/10.1029/2002GL015314. https://agupubs.onlinelibrary.wiley.com/doi/pdf/10.1029/2002GL015314 .

Ripin, B.H., E.A. McLean, C.K. Manka, C. Pawley, and J.A. Stamper. 1987, November. Large-Larmor-radius interchange instability. *Physical Review Letters* 59: 2299–2302. https://doi.org/10.1103/PhysRevLett.59.2299 .

Rogers, B.N., R.E. Denton, J.F. Drake, and M.A. Shay. 2001, October. Role of Dispersive Waves in Collisionless Magnetic Reconnection. *Physical Review Letters 87* (19): 195004. https://doi.org/10.1103/PhysRevLett.87.195004 .

Runov, A., R. Nakamura, and W. Baumjohann. 2006, January. Multi-point study of the magnetotail current sheet. *Advances in Space Research 38* (1): 85–92. https://doi.org/10.1016/j.asr.2004.09.024 .

Russell, C.T., R.J. Strangeway, C. Zhao, B.J. Anderson, W. Baumjohann, K.R. Bromund, D. Fischer, L. Kepko, G. Le, W. Magnes, R. Nakamura, F. Plaschke, J.A. Slavin, R.B. Torbert, T.E. Moore, W.R. Paterson, C.J. Pollock, and J.L. Burch. 2017, June. Structure, force balance, and topology of Earth's magnetopause. *Science* 356: 960–963. https://doi.org/10.1126/science.aag3112 .

Sakai, K., S. Isayama, N. Bolouki, M.S. Habibi, Y.L. Liu, Y.H. Hsieh, H.H. Chu, J. Wang, S.H. Chen, T. Morita, K. Tomita, R. Yamazaki, Y. Sakawa, S. Matsukiyo, and Y. Kuramitsu. 2020. Collective thomson scattering in non-equilibrium laser produced two-stream plasmas. *Physics of Plasmas 27* (10): 103104. https://doi.org/10.1063/5.0011935. https://doi.org/10.1063/5.0011935 .

Sakai, K., T. Moritaka, T. Morita, K. Tomita, T. Minami, T. Nishimoto, S. Egashira, M. Ota, Y. Sakawa, N. Ozaki, R. Kodama, T. Kojima, T. Takezaki, R. Yamazaki, S.J. Tanaka, K. Aihara, M. Koenig, B. Albertazzi, P. Mabey, N. Woolsey, S. Matsukiyo, H. Takabe, M. Hoshino, and Y. Kuramitsu. 2022. Direct observations of pure electron outflow in magnetic reconnection. *Scientific Reports 12*(1): 10921. https://doi.org/10.1038/s41598-022-14582-3 .

Sakai, K., T. Nishimoto, S. Isayama, S. Matsukiyo, and Y. Kuramitsu. 2023. Ion-acoustic feature of collective thomson scattering in non-equilibrium two-stream plasmas. *Physics of Plasmas 30*(1): 012105. https://doi.org/10.1063/5.0117812. https://doi.org/10.1063/5.0117812 .

Sang, L., Q. Lu, J. Xie, F. Fan, Q. Zhang, W. Ding, J. Zheng, and X. Sun. 2022, 10. Energy dissipation during magnetic reconnection in the Keda linear magnetized plasma device. *Physics of Plasmas 29*(10). https://doi.org/10.1063/5.0090790. https://pubs.aip.org/aip/pop/article-pdf/doi/10.1063/5.0090790/16570733/102108_1_online.pdf .

Sato, T. and T. Hayashi. 1979. Externally driven magnetic reconnection and a powerful magnetic energy converter. *Physics of Fluids 22*(6): 1189. https://doi.org/10.1063/1.862721 .

Schaeffer, D.B., A.F.A. Bott, M. Borghesi, K.A. Flippo, W. Fox, J. Fuchs, C. Li, H.S. Park, F.H. Seguin, P. Tzeferacos, and L. Willingale. 2022, December. Proton Imaging of High-Energy-Density Laboratory Plasmas.

Sergeev, V., A. Runov, W. Baumjohann, R. Nakamura, T.L. Zhang, A. Balogh, P. Louarnd, J.A. Sauvaud, and H. Reme. 2004, March. Orientation and propagation of current sheet oscillations. *Geophysical Research Letters 31*(5). https://doi.org/10.1029/2003GL019346 .

Sergeev, V.A., V. Angelopoulos, D.G. Mitchell, and C.T. Russell. 1995. In situ observations of magnetotail reconnection prior to the onset of a small substorm. *Journal of Geophysical Research 100*(A10): 19121. https://doi.org/10.1029/95JA01471 .

Sharma Pyakurel, P., M.A. Shay, T.D. Phan, W.H. Matthaeus, J.F. Drake, J.M. TenBarge, C.C. Haggerty, K.G. Klein, P.A. Cassak, T.N. Parashar, M. Swisdak, and A. Chasapis. 2019, 08. Transition from ion-coupled to electron-only reconnection: Basic physics and implications for plasma turbulence. *Physics of Plasmas 26*(8): 082307. https://doi.org/10.1063/1.5090403. https://pubs.aip.org/aip/pop/article-pdf/doi/10.1063/1.5090403/15852665/082307_1_online.pdf .

Shay, M.A., J.F. Drake, B.N. Rogers, and R.E. Denton. 2001, March. Alfvénic collisionless magnetic reconnection and the Hall term. *Journal of Geophysical Research: Space Physics 106*(A3): 3759–3772. https://doi.org/10.1029/1999JA001007 .

Shay, M.A., J.F. Drake, and M. Swisdak. 2007, October. Two-Scale Structure of the Electron Dissipation Region during Collisionless Magnetic Reconnection. *Physical Review Letters 99*(15): 155002. https://doi.org/10.1103/PhysRevLett.99.155002 .

Shi, P., P. Srivastav, M.H. Barbhuiya, P.A. Cassak, E.E. Scime, and M. Swisdak. 2022, Jan. Laboratory observations of electron heating and non-maxwellian distributions at the kinetic scale during electron-only magnetic reconnection. *Phys. Rev. Lett.* 128: 025002. https://doi.org/10.1103/PhysRevLett.128.025002 .

Shi, P., P. Srivastav, M.H. Barbhuiya, P.A. Cassak, E.E. Scime, M. Swisdak, C. Beatty, T. Gilbert, R. John, M. Lazo, R.S. Nirwan, M. Paul, E.E. Scime, K. Stevenson, and T. Steinberger. 2022. Electron-only reconnection and associated electron heating and acceleration in phasma. *Physics of Plasmas 29*(3): 032101. https://doi.org/10.1063/5.0082633 .

Shinohara, I., T. Nagai, M. Fujimoto, T. Terasawa, T. Mukai, K. Tsuruda, and T. Yamamoto. 1998, September. Low-frequency electromagnetic turbulence observed near the substorm onset site. *Journal of Geophysical Research: Space Physics 103*(A9): 20365–20388. https://doi.org/10.1029/98JA01104 .

Shuster, J.R., L.J. Chen, W.S. Daughton, L.C. Lee, K.H. Lee, N. Bessho, R.B. Torbert, G. Li, and M.R. Argall. 2014, August. Highly structured electron anisotropy in collisionless reconnection exhausts. *Geophysical Research Letters 41*(15): 5389–5395. https://doi.org/10.1002/2014GL060608 .

Silin, I. and J. Büchner. 2003, May. Kinetic instabilities of thin current sheets: Results of two-and-one-half-dimensional Vlasov code simulations. *Physics of Plasmas 10*(5): 1299–1307. https://doi.org/10.1063/1.1561275 .

Silin, I., J. Büchner, and A. Vaivads. 2005, June. Anomalous resistivity due to nonlinear lower-hybrid drift waves. *Physics of Plasmas 12*(6): 062902. https://doi.org/10.1063/1.1927096 .

Smith, M.F. and D.J. Rodgers. 1991. Ion distributions at the dayside magnetopause. *Journal of Geophysical Research 96*(A7): 11617. https://doi.org/10.1029/91JA00676 .

Stamper, J.A. 1991, 11. Review on spontaneous magnetic fields in laser-produced plasmas: Phenomena and measurements. *Laser and Particle Beams* 9: 841–862. https://doi.org/10.1017/S0263034600006595 .

Stamper, J.A., K. Papadopoulos, R.N. Sudan, S.O. Dean, E.A. McLean, and J.M. Dawson. 1971, April. Spontaneous Magnetic Fields in Laser-Produced Plasmas. *Physical Review Letters* 26: 1012–1015. https://doi.org/10.1103/PhysRevLett.26.1012 .

Stamper, J.A. and B.H. Ripin. 1975, January. Faraday-rotation measurements of megagauss magnetic fields in laser-produced plasmas. *Physical Review Letters* 34: 138–141 .

Stawarz, J.E., J.P. Eastwood, T.D. Phan, I.L. Gingell, M.A. Shay, J.L. Burch, R.E. Ergun, B.L. Giles, D.J. Gershman, O.L. Contel, P.A. Lindqvist, C.T. Russell, R.J. Strangeway, R.B. Torbert, M.R. Argall, D. Fischer, W. Magnes, and L. Franci. 2019, jun. Properties of the turbulence associated with electron-only magnetic reconnection in earth's magnetosheath. *The Astrophysical Journal Letters* *877*(2): L37. https://doi.org/10.3847/2041-8213/ab21c8 .

Sundkvist, D., A. Retinò, A. Vaivads, and S.D. Bale. 2007, Jul. Dissipation in turbulent plasma due to reconnection in thin current sheets. *Phys. Rev. Lett.* 99: 025004. https://doi.org/10.1103/PhysRevLett.99.025004 .

Sweet, P. 1958, 01. The neutral point theory of solar flares. *Symposium - International Astronomical Union* 6: 123. https://doi.org/10.1017/S0074180900237704 .

Takabe, H. and Y. Kuramitsu. 2021. Recent progress of laboratory astrophysics with intense lasers. *High Power Laser Science and Engineering* 9: e49. https://doi.org/10.1017/hpl.2021.35 .

Torbert, R.B., J.L. Burch, T.D. Phan, M. Hesse, M.R. Argall, J. Shuster, R.E. Ergun, L. Alm, R. Nakamura, K.J. Genestreti, D.J. Gershman, W.R. Paterson, D.L. Turner, I. Cohen, B.L. Giles, C.J. Pollock, S. Wang, L.J. Chen, J.E. Stawarz, J.P. Eastwood, K.J. Hwang, C. Farrugia, I. Dors, H. Vaith, C. Mouikis, A. Ardakani, B.H. Mauk, S.A. Fuselier, C.T. Russell, R.J. Strangeway, T.E. Moore, J.F. Drake, M.A. Shay, Y.V. Khotyaintsev, P.A. Lindqvist, W. Baumjohann, F.D. Wilder, N. Ahmadi, J.C. Dorelli, L.A. Avanov, M. Oka, D.N. Baker, J.F. Fennell, J.B. Blake, A.N. Jaynes, O. Le Contel, S.M. Petrinec, B. Lavraud, and Y. Saito. 2018. Electron-scale dynamics of the diffusion region during symmetric magnetic reconnection in space. *Science* *362*(6421): 1391–1395. https://doi.org/10.1126/science.aat2998. https://science.sciencemag.org/content/362/6421/1391.full.pdf .

Torbert, R.B., J.L. Burch, T.D. Phan, M. Hesse, M.R. Argall, J. Shuster, R.E. Ergun, L. Alm, R. Nakamura, K.J. Genestreti, D.J. Gershman, W.R. Paterson, D.L. Turner, I. Cohen, B.L. Giles, C.J. Pollock, S. Wang, L.J. Chen, J.E. Stawarz, J.P. Eastwood, K.J. Hwang, C. Farrugia, I. Dors, H. Vaith, C. Mouikis, A. Ardakani, B.H. Mauk, S.A. Fuselier, C.T. Russell,

R.J. Strangeway, T.E. Moore, J.F. Drake, M.A. Shay, Y.V. Khotyaintsev, P.A. Lindqvist, W. Baumjohann, F.D. Wilder, N. Ahmadi, J.C. Dorelli, L.A. Avanov, M. Oka, D.N. Baker, J.F. Fennell, J.B. Blake, A.N. Jaynes, O.L. Contel, S.M. Petrinec, B. Lavraud, and Y. Saito. 2018. Electron-scale dynamics of the diffusion region during symmetric magnetic reconnection in space. *Science 362*(6421): 1391–1395. https://doi.org/10.1126/science. aat2998. https://www.science.org/doi/pdf/10.1126/science.aat2998 .

Tsuneta, S., K. Ichimoto, Y. Katsukawa, S. Nagata, M. Otsubo, T. Shimizu, Y. Suematsu, M. Nakagiri, M. Noguchi, T. Tarbell, A. Title, R. Shine, W. Rosenberg, C. Hoffmann, B. Jurcevich, G. Kushner, M. Levay, B. Lites, D. Elmore, T. Matsushita, N. Kawaguchi, H. Saito, I. Mikami, L.D. Hill, and J.K. Owens. 2009. The Solar Optical Telescope for the Hinode Mission: An Overview, In *The Hinode Mission*, ed. Sakurai, T., 113–142. New York, NY: Springer New York. https://doi.org/10.1007/978-0-387-88739-5_8.

Usami, S. and R. Horiuchi. 2022, March. Pseudo-Maxwellian Velocity Distribution Formed by the Pickup-like Process in Magnetic Reconnection. *Frontiers in Astronomy and Space Sciences* 9: 846395. https://doi.org/10.3389/fspas. 2022.846395 .

Usami, S., R. Horiuchi, H. Ohtani, and M. Den. 2013, June. Development of multi-hierarchy simulation model with non-uniform space grids for collisionless driven reconnection. *Physics of Plasmas 20*(6): 061208. https://doi. org/10.1063/1.4811121 .

Vaivads, A., Y. Khotyaintsev, M. André, A. Retinò, S. Buchert, B. Rogers, P. Décréau, G. Paschmann, and T. Phan. 2004, August. Structure of the Magnetic Reconnection Diffusion Region from Four-Spacecraft Observations. *Physical Review Letters 93*(10): 105001. https://doi.org/10.1103/ PhysRevLett.93.105001 .

Vanzeeland, M. and W. Gekelman. 2004, January. Laser-plasma diamagnetism in the presence of an ambient magnetized plasma. *Physics of Plasmas* 11: 320–323. https://doi.org/10.1063/1.1628233 .

Vörös, Z., E. Yordanova, A. Varsani, K.J. Genestreti, Y.V. Khotyaintsev, W. Li, D.B. Graham, C. Norgren, R. Nakamura, Y. Narita, F. Plaschke, W. Magnes, W. Baumjohann, D. Fischer, A. Vaivads, E. Eriksson, P.A. Lindqvist, G. Marklund, R.E. Ergun, M. Leitner, M.P. Leubner, R.J. Strangeway, O. Le Contel, C. Pollock, B.J. Giles, R.B. Torbert, J.L. Burch, L.A. Avanov, J.C. Dorelli, D.J. Gershman, W.R. Paterson, B. Lavraud, and Y. Saito. 2017. Mms observation of magnetic reconnection in the turbulent magnetosheath. *Journal of Geophysical Research: Space Physics 122*(11): 11,442–11,467. https://doi.org/https://doi.org/10.1002/ 2017JA024535. https://agupubs.onlinelibrary.wiley.com/doi/pdf/10.1002/ 2017JA024535 .

Vekstein, G. 2017, October. Forced magnetic reconnection. *Journal of Plasma Physics 83*(5): 205830501. https://doi.org/10.1017/S0022377817000782 .

Wang, R., Q. Lu, S. Lu, C.T. Russell, J.L. Burch, D.J. Gershman, W. Gonzalez, and S. Wang. 2020. Physical implication of two types of reconnection electron diffusion regions with and without ion-coupling in the magnetotail current sheet. *Geophysical Research Letters 47*(21): e2020GL088761. https://doi.org/https://doi.org/10.1029/2020GL088761. https://agupubs.onlinelibrary.wiley.com/doi/pdf/10.1029/2020GL088761 .

Wang, R., Q. Lu, R. Nakamura, W. Baumjohann, C. Huang, C.T. Russell, J.L. Burch, C.J. Pollock, D. Gershman, R.E. Ergun, S. Wang, P.A. Lindqvist, and B. Giles. 2018. An electron-scale current sheet without bursty reconnection signatures observed in the near-earth tail. *Geophysical Research Letters 45*(10): 4542–4549. https://doi.org/https://doi.org/10.1002/2017GL076330. https://agupubs.onlinelibrary.wiley.com/doi/pdf/10.1002/2017GL076330 .

Wang, R., R. Nakamura, Q. Lu, W. Baumjohann, R.E. Ergun, J.L. Burch, M. Volwerk, A. Varsani, T. Nakamura, W. Gonzalez, B. Giles, D. Gershman, and S. Wang. 2017, Apr. Electron-scale quadrants of the hall magnetic field observed by the magnetospheric multiscale spacecraft during asymmetric reconnection. *Phys. Rev. Lett.* 118: 175101. https://doi.org/10.1103/PhysRevLett.118.175101 .

Wang, S., R. Wang, Q. Lu, C.T. Russell, R.E. Ergun, and S. Wang. 2021. Large-scale parallel electric field colocated in an extended electron diffusion region during the magnetosheath magnetic reconnection. *Geophysical Research Letters 48*(23): e2021GL094879. https://doi.org/https://doi.org/10.1029/2021GL094879. https://agupubs.onlinelibrary.wiley.com/doi/pdf/10.1029/2021GL094879 .

Wilder, F.D., R.E. Ergun, J.L. Burch, N. Ahmadi, S. Eriksson, T.D. Phan, K.A. Goodrich, J. Shuster, A.C. Rager, R.B. Torbert, B.L. Giles, R.J. Strangeway, F. Plaschke, W. Magnes, P.A. Lindqvist, and Y.V. Khotyaintsev. 2018. The role of the parallel electric field in electron-scale dissipation at reconnecting currents in the magnetosheath. *Journal of Geophysical Research: Space Physics 123*(8): 6533–6547. https://doi.org/https://doi.org/10.1029/2018JA025529. https://agupubs.onlinelibrary.wiley.com/doi/pdf/10.1029/2018JA025529 .

Wilder, F.D., R.E. Ergun, S. Eriksson, T.D. Phan, J.L. Burch, N. Ahmadi, K.A. Goodrich, D.L. Newman, K.J. Trattner, R.B. Torbert, B.L. Giles, R.J. Strangeway, W. Magnes, P.A. Lindqvist, and Y.V. Khotyaintsev. 2017, June. Multipoint Measurements of the Electron Jet of Symmetric Magnetic Reconnection with a Moderate Guide Field. *Physical Review Letters 118*(26):

265101. https://doi.org/10.1103/PhysRevLett.118.265101 .

Winske, D. 1981. Current-driven microinstabilities in a neutral sheet. *Physics of Fluids* *24*(6): 1069. https://doi.org/10.1063/1.863485 .

Woolsey, N.C., Y.A. Ali, R.G. Evans, R.A.D. Grundy, S.J. Pestehe, P.G. Carolan, N.J. Conway, R.O. Dendy, P. Helander, K.G. McClements, J.G. Kirk, P.A. Norreys, M.M. Notley, and S.J. Rose. 2001, May. Collisionless shock and supernova remnant simulations on VULCAN. *Physics of Plasmas* 8: 2439–2445. https://doi.org/10.1063/1.1351831 .

Yamada, M. 2022. *Magnetic Reconnection: A Modern Synthesis of Theory, Experiment, and Observations*, Volume 61. Princeton University Press.

Yamada, M., L.J. Chen, J. Yoo, S. Wang, W. Fox, J. Jara-Almonte, H. Ji, W. Daughton, A. Le, J. Burch, B. Giles, M. Hesse, T. Moore, and R. Torbert. 2018, December. The two-fluid dynamics and energetics of the asymmetric magnetic reconnection in laboratory and space plasmas. *Nature Communications* *9*(1): 5223. https://doi.org/10.1038/s41467-018-07680-2 .

Yamada, M., R. Kulsrud, and H. Ji. 2010, Mar. Magnetic reconnection. *Rev. Mod. Phys.* 82: 603–664. https://doi.org/10.1103/RevModPhys.82.603 .

Yamada, M., Y. Ren, H. Ji, J. Breslau, S. Gerhardt, R. Kulsrud, and A. Kuritsyn. 2006, May. Experimental study of two-fluid effects on magnetic reconnection in a laboratory plasma with variable collisionality. *Physics of Plasmas* *13*(5): 052119. https://doi.org/10.1063/1.2203950 .

Yamada, M., J. Yoo, J. Jara-Almonte, H. Ji, R.M. Kulsrud, and C.E. Myers. 2014. Conversion of magnetic energy in the magnetic reconnection layer of a laboratory plasma. *Nature Communications* *5*(1): 4774. https://doi.org/10.1038/ncomms5774 .

Yamazaki, R., S. Matsukiyo, T. Morita, S.J. Tanaka, T. Umeda, K. Aihara, M. Edamoto, S. Egashira, R. Hatsuyama, T. Higuchi, T. Hihara, Y. Horie, M. Hoshino, A. Ishii, N. Ishizaka, Y. Itadani, T. Izumi, S. Kambayashi, S. Kakuchi, N. Katsuki, R. Kawamura, Y. Kawamura, S. Kisaka, T. Kojima, A. Konuma, R. Kumar, T. Minami, I. Miyata, T. Moritaka, Y. Murakami, K. Nagashima, Y. Nakagawa, T. Nishimoto, Y. Nishioka, Y. Ohira, N. Ohnishi, M. Ota, N. Ozaki, T. Sano, K. Sakai, S. Sei, J. Shiota, Y. Shoji, K. Sugiyama, D. Suzuki, M. Takagi, H. Toda, S. Tomita, S. Tomiya, H. Yoneda, T. Takezaki, K. Tomita, Y. Kuramitsu, and Y. Sakawa. 2022, Feb. High-power laser experiment forming a supercritical collisionless shock in a magnetized uniform plasma at rest. *Phys. Rev. E* 105: 025203. https://doi.org/10.1103/PhysRevE.105.025203 .

Yates, M.A., D.B. van Hulsteyn, H. Rutkowski, G. Kyrala, and J.U. Brackbill. 1982, Dec. Experimental evidence for self-generated magnetic fields and remote energy deposition in laser-irradiated targets. *Phys. Rev. Lett.* 49: 1702–1704. https://doi.org/10.1103/PhysRevLett.49.1702 .

Yin, L., W. Daughton, H. Karimabadi, B.J. Albright, K.J. Bowers, and J. Margulies. 2008, September. Three-Dimensional Dynamics of Collisionless Magnetic Reconnection in Large-Scale Pair Plasmas. *Physical Review Letters 101*(12): 125001. https://doi.org/10.1103/PhysRevLett.101.125001 .

Yoon, P.H., A.T.Y. Lui, and M.I. Sitnov. 2002, May. Generalized lower-hybrid drift instabilities in current-sheet equilibrium. *Physics of Plasmas 9*(5): 1526–1538. https://doi.org/10.1063/1.1466822 .

Yoon, Y.D. and P.M. Bellan. 2017, May. A generalized two-fluid picture of non-driven collisionless reconnection and its relation to whistler waves. *Physics of Plasmas 24*(5): 052114. https://doi.org/10.1063/1.4982812 .

Yordanova, E., Z. Vörös, A. Varsani, D.B. Graham, C. Norgren, Y.V. Khotyaintsev, A. Vaivads, E. Eriksson, R. Nakamura, P.A. Lindqvist, G. Marklund, R.E. Ergun, W. Magnes, W. Baumjohann, D. Fischer, F. Plaschke, Y. Narita, C.T. Russell, R.J. Strangeway, O. Le Contel, C. Pollock, R.B. Torbert, B.J. Giles, J.L. Burch, L.A. Avanov, J.C. Dorelli, D.J. Gershman, W.R. Paterson, B. Lavraud, and Y. Saito. 2016. Electron scale structures and magnetic reconnection signatures in the turbulent magnetosheath. *Geophysical Research Letters 43*(12): 5969–5978. https://doi.org/https://doi.org/10.1002/2016GL069191. https://agupubs.onlinelibrary.wiley.com/doi/pdf/10.1002/2016GL069191 .

Zenitani, S., M. Hesse, A. Klimas, and M. Kuznetsova. 2011, May. New Measure of the Dissipation Region in Collisionless Magnetic Reconnection. *Physical Review Letters 106*(19): 195003. https://doi.org/10.1103/PhysRevLett.106.195003. arXiv:1104.3846 [astro-ph.SR].

Zhang, Q., F. Guo, W. Daughton, H. Li, and X. Li. 2021, October. Efficient Nonthermal Ion and Electron Acceleration Enabled by the Flux-Rope Kink Instability in 3D Nonrelativistic Magnetic Reconnection. *Physical Review Letters 127*(18): 185101. https://doi.org/10.1103/PhysRevLett.127.185101 .

Zhong, J., Y. Li, X. Wang, J. Wang, Q. Dong, C. Xiao, S. Wang, X. Liu, L. Zhang, L. An, F. Wang, J. Zhu, Y. Gu, X. He, G. Zhao, and J. Zhang. 2010, December. Modelling loop-top X-ray source and reconnection outflows in solar flares with intense lasers. *Nature Physics* 6: 984–987. https://doi.org/10.1038/nphys1790 .

Zhong, J., X. Yuan, B. Han, W. Sun, and Y. Ping. 2018, 3. Magnetic reconnection driven by intense lasers. *High Power Laser Science and Engineering 6*(11): 03000e48 .

Zhu, Z. and R.M. Winglee. 1996, March. Tearing instability, flux ropes, and the kinetic current sheet kink instability in the Earth's magnetotail: A three-dimensional perspective from particle simulations. *Journal of Geophysical Research: Space Physics 101*(A3): 4885–4897. https://doi.org/10.1029/95JA03144 .

Zweibel, E.G. and M. Yamada. 2009, September. Magnetic Reconnection in Astrophysical and Laboratory Plasmas. *Annual Review of Astronomy and Astrophysics 47*(1): 291–332. https://doi.org/10.1146/annurev-astro-082708-101726 .